

Two-point sum-rules in three-dimensional Yang-Mills theory

Simon Caron-Huot^a Andrzej Pokraka^b Zahra Zahraee^{a,c}

^a*Department of Physics, McGill University, 3600 Rue University, Montréal, Canada*

^b*Department of Physics, Brown University, Providence, RI 02912, USA*

^c*CERN, Theoretical Physics Department, CH-1211 Geneva 23, Switzerland*

E-mail: schuot@physics.mcgill.ca, andrzej_pokraka@brown.edu,
zahra.zahraee@cern.ch

ABSTRACT: We compute the stress-tensor two-point function in three-dimensional Yang-Mills theory to three-loops in perturbation theory. Using its calculable shape at high momenta, we test the notion that its Borel transform is saturated at low energies by the lowest glueball state(s). This assumption provides relatively stable estimates for the mass of the lightest glueball that we compare with lattice simulations. We also provide estimates for the coupling of the lightest glueball to the stress tensor. Along the way, we comment on the extent that such estimates are non-rigorous. Lastly, we discuss the possibility of applying the sum-rule analysis to two-point functions of higher-spin operators and obtain a crude approximation for the glueball couplings to these operators.

Contents

1	Introduction	2
2	Stress-energy tensor two-point function	3
2.1	One-loop two-point functions	6
2.2	One- and two-loop two-point functions via the unitarity method	7
2.3	Two- and three-loop two-point functions	9
2.4	Superconvergent combination of two-point functions	10
3	Sum-rules: estimating the glueball masses and couplings	12
3.1	Dispersion relations	12
3.2	Borel transformation	14
3.3	Borel transformation of the perturbative result	15
3.4	Borel transformation of the non-perturbative model	16
3.5	One-glueball model ($N = 1$)	17
3.6	Two-glueball model ($N = 2$)	18
3.7	Comparison with lattice data	22
4	Everything is consistent with unitarity!	23
5	Higher-spin currents	25
5.1	Higher-spin Correlation Functions	25
5.2	Basis for higher-spin Operators	27
5.3	One- and two-loop with unitarity method	28
5.4	Two-loop higher-spin correlators	29
5.5	Superconvergent Combinations	29
6	Conclusions	31
A	d-dimensional form factors	32
A.1	One-loop	32
A.2	Two-loops	33
A.3	Three-loops	33
B	Computing $I_1^{(3)}$ and $I_2^{(3)}$ from dimensional recurrence	35
B.1	Dimensional recurrence and analyticity in d	35
B.2	Computing $I_1^{(3)}$ and $I_2^{(3)}$	37
C	Ingredients for on-shell calculations	38
C.1	Stress-Tensor gluon form factors	39
C.2	Phase space integrals	39

1 Introduction

Understanding the non-perturbative dynamics of strongly coupled systems from first principles has been a long standing problem in modern quantum field theory (QFT). Arguably, the most direct calculation of non-perturbative effects come from lattice simulations where one computes QFT correlation functions in a discretized spacetime and then extrapolates to the continuum. While less direct, one can also obtain some non-perturbative information through dispersion relations that connect correlators at large (computable) space-like momenta and small momenta, as in the famous QCD sum-rules [1–4]. Surprisingly, the low energy contribution to these sum-rules is often found to be numerically dominated by the lightest bound states, yielding estimates of their various properties. In light of the continuing interest in rigorous results on confining theories, we would like to revisit these old ideas in the context of three-dimensional Yang-Mills theory, where both perturbative calculations and lattice simulations are possible.

The central object of our study will be the stress-energy 2-point function

$$\Pi^{\mu\nu\alpha\beta}(p^2) = i \int d^d x e^{-ip \cdot x} \langle 0 | \mathbb{T} \{ T^{\mu\nu}(x) T^{\alpha\beta}(0) \} | 0 \rangle, \quad (1.1)$$

which probes intermediate glueball states $|G\rangle$ through its imaginary/absorptive part

$$\begin{aligned} 2\text{Im} \Pi^{\mu\nu\alpha\beta}(p^2) &= \int d^d x e^{-ip \cdot x} \langle 0 | T^{\mu\nu}(x) T^{\alpha\beta}(0) | 0 \rangle \\ &= \int d^d x e^{-ip \cdot x} \not\int_G \langle 0 | T^{\mu\nu}(x) | G \rangle \langle G | T^{\alpha\beta}(0) | 0 \rangle. \end{aligned} \quad (1.2)$$

Like any two-point correlator, $\Pi^{\mu\nu\alpha\beta}$ in (1.1) admits a Källén-Lehmann dispersion relation that expresses it as an integral over a spectral density (1.2). The latter consists of two non-negative functions, corresponding to spin-0 and spin-2 exchanges. On the one hand, at large Euclidean momenta the correlator can be calculated using perturbation theory. On the other hand, the qualitative features of the spectral density are known at low energies: we expect a sum of δ -function contributions from stable glueballs followed by a continuum that possibly includes further resonances. The goal of this work is to explore the consequences of the dispersion relation that connects these quantities.

One of our motivations is recent work on the S-matrix bootstrap [5, 6] in which scattering amplitudes of stable bound states are supplemented by form factors and two-point functions of local operators, in order to rigorously connect short- and large-distance physics. Here, we focus only on two-point functions and numerically explore less rigorous connections in the spirit of QCD sum-rules. Three-dimensional Yang-Mills is a natural model to study from this perspective since it is super-renormalizable (i.e., amenable to perturbation theory) and has interesting non-perturbative dynamics (i.e., confinement). The presence of a (perturbative) mass scale in three-dimensional Yang-Mills theory is an additional simplification with respect to QCD where the mass scale is provided by non-perturbative condensates. At the same time, three-dimensional Yang-Mills theory (especially without fermions) is readily amenable to lattice simulations and excellent data exists on its spectrum [7–20].

Concretely, we will calculate the stress-tensor correlator (1.1) in pure three-dimensional Yang-Mills theory to three-loop order in perturbation theory. Following traditional sum-rules

approach, we then apply a Borel transform with respect to energy to improve convergence (see equation (3.11) below). The main question is whether the Borel transform is dominated at low energies by the lightest glueball(s). We test this by assuming it is true and seeing whether it predicts reasonable values for the lowest glueball mass and its coupling to the stress tensor. The former is then compared with known lattice results, while the latter (to our knowledge) is a prediction.

In principle, this method can also be extended to higher-spin operators. Knowing the set of couplings $\langle G|\mathcal{O}^\ell|0\rangle$ of a given glueball to minimal-twist operators of various spins amounts to knowing its so-called lightcone wavefunction. This wavefunction is closely related but distinct from parton distribution functions (which control deep inelastic scattering at high energies) in that it controls elastic scattering at high energies [21–23]. In the QCD context, such quantities have been estimated using sum-rules for higher-spin currents [24]. We initiate the investigation of higher-spin sum-rules for three-dimensional Yang-Mills theory.

In section 2, we describe the stress-energy two-point function and provide some details of our 3-loop calculation. While we quote only its three-dimensional limit in the main text, the d -dimensional results can be found in appendix A. Up to two-loops, we include cross-checks on the imaginary part using on-shell methods. In section 3, we review Borel-transformed sum-rules for two-point functions and use simple models for the spectral density to extract the glueball masses and couplings from a χ^2 -fit. We also comment on the comparison with lattice results. These estimates are not rigorous and we explain in section 4 that essentially any low-energy spectral density can be compatible with perturbative asymptotics. Lastly, in section 5, we compute the perturbative two-point functions of more general higher-spin operators and show the existence of “superconvergent” sum-rules. This analysis leads to a crude approximation of glueball couplings to these operators.

2 Stress-energy tensor two-point function

In this section, we review our conventions for the YM-Lagrangian and define the stress-energy two-point functions relevant to this work. We compute the spin-0 and spin-2 two-point functions at one-loop in section 2.1. In section 2.2, we cross-check the discontinuities of one-loop two-point functions and predict the two-loop discontinuities from unitarity cuts. Then, we compute the full two-point functions at two- and three-loops in section 2.3. In section 2.4, we identify a combination of the two-point functions with particularly good behaviour near $p^2 = 0$. This “superconvergent” combination will be central to the sum-rule analysis of section 3.

The YM Lagrangian is comprised of three parts: a pure YM Lagrangian \mathcal{L}_{YM} , a gauge fixing condition \mathcal{L}_{gf} and a ghost Lagrangian \mathcal{L}_{gh} . Explicitly, the total Lagrangian is (we work in mostly-plus metric signature) is

$$\mathcal{L} = -\frac{1}{4g_s^2} (F_{\mu\nu}^a)^2 + \mathcal{L}_{\text{gf}} + \mathcal{L}_{\text{gh}} \quad (2.1)$$

where

$$F_{\mu\nu}^a = \partial_\mu A_\nu^a - \partial_\nu A_\mu^a + f^{abc} A_\mu^b A_\nu^c \quad (2.2)$$

is the YM field strength. Since we will eventually specialize to $d = 3$ spacetime dimensions rather than four, it is useful to compare the mass dimension of the coupling constant:

$$[g_s^2] = 4 - d \rightarrow \begin{cases} 0 & \text{for } d = 4, \\ 1 & \text{for } d = 3. \end{cases} \quad (2.3)$$

Comparing, we see that the coupling constant provides a natural scale in three-dimensions but not in four-dimensions. This is one of the main reasons we will be interested in $d = 3$ in this work: confinement and the bound state spectrum is controlled by the scale $m \sim g_s^2 C_A$ instead of being an inherently non-perturbative function of the cut off Λ_{QCD} in four dimensions.

The stress-energy tensor is given by the expression

$$T^{\mu\nu} = \frac{1}{g_s^2} \left((F^a)^{\mu\lambda} (F^a)^\nu{}_\lambda - \frac{1}{4} g^{\mu\nu} F^2 \right). \quad (2.4)$$

Since the $SU(N_c)$ gauge theory admits parity and charge conjugation symmetries, the spectral decomposition (1.2) admits the group theoretic expansion

$$\text{Im } \Pi^{\mu\nu\alpha\beta}(p^2) \propto \sum_{J,P,C} \langle 0 | T^{\mu\nu}(p^2) | G_J^{PC} \rangle \langle G_J^{PC} | T^{\alpha\beta}(p^2) | 0 \rangle \quad (2.5)$$

where the overlap $\langle G_{J=0,2}^{++} | T^{\mu\nu}(p^2) | 0 \rangle \neq 0$ is only nonvanishing for spins $J = 0, 2$ and $PC = ++$.¹ In section 3, we will try to use its two-point function to extract approximations for the masses and couplings of the lowest-lying glueball states.

The stress-energy tensor two-point function has four hanging Lorentz indices. The Ward identities imply that a certain combination is transverse with respect to the external momentum p (see [25]):

$$p_\mu \left(\Pi^{\mu\nu\alpha\beta}(p^2) + g^{\nu\alpha} \langle T^{\mu\beta} \rangle + g^{\nu\beta} \langle T^{\mu\alpha} \rangle - g^{\mu\nu} \langle T^{\alpha\beta} \rangle \right) = 0. \quad (2.6)$$

We focus on the vacuum state, where all the above objects are constrained by Lorentz invariance. There are only two transverse tensor structures with four Lorentz indices that are symmetric in each pair:

$$\phi_0^{\mu\nu\alpha\beta}(p) \equiv \phi^{\mu\nu} \phi^{\alpha\beta}, \quad (2.7)$$

$$\phi_2^{\mu\nu\alpha\beta}(p) \equiv \phi^{\mu\alpha} \phi^{\nu\beta} + \phi^{\mu\beta} \phi^{\nu\alpha} - c_d \phi^{\mu\nu} \phi^{\alpha\beta}, \quad (2.8)$$

where $c_d = \frac{2}{d-1}$ and

$$\phi^{\mu\nu}(p) \equiv \left(g^{\mu\nu} - \frac{p^\mu p^\nu}{p^2} \right). \quad (2.9)$$

¹In $2+1$ spacetime dimensions, parity P is a reflection $(x, y, t) \mapsto (-x, y, t)$ which anticommutes with the angular momentum of a particle. Thus any massive particle of spin $J \neq 0$ comes in a degenerate multiplet $\{|J\rangle, |-J\rangle\}$. Since any such multiplet is unitarily equivalent, the P superscript is only meaningful (in the continuum theory) for $J = 0$ states, see [8] for discussion.

Consequently, the general solution, $\Pi^{\mu\nu\alpha\beta}$, to the Ward identities (2.6) has a simple form:

$$\begin{aligned} \Pi^{\mu\nu\alpha\beta}(p^2) &= \frac{d_G}{512} \left[A_0(p^2) \phi_0^{\mu\nu\alpha\beta}(p) + A_2(p^2) \phi_2^{\mu\nu\alpha\beta}(p) \right] \\ &+ (g^{\mu\alpha} g^{\nu\beta} + g^{\mu\beta} g^{\nu\alpha} - g^{\mu\nu} g^{\alpha\beta}) \Lambda, \end{aligned} \quad (2.10)$$

where we have set $\langle T^{\mu\nu} \rangle = -\Lambda \delta^{\mu\nu}$. For future convenience, we have absorbed a numerical factor as well as a factor of d_G : the dimension of the gauge group ($d_G = N_c^2 - 1$ for $G = SU(N_c)$). The value of c_d was chosen so that the spin-2 structure is traceless in each pair, which also makes it orthogonal to ϕ_0 :

$$(\phi_2)_{\mu}^{\mu\alpha\beta} = 0 = (\phi_2)^{\mu\nu\alpha}_{\alpha}, \quad \phi_0^{\mu\nu\alpha\beta} (\phi_2)_{\alpha\beta\mu\nu} = 0. \quad (2.11)$$

Therefore, the two-point functions $A_0(p^2)$ and $A_2(p^2)$ receive contributions from only spin-0 and spin-2 intermediate states in the group theory decomposition (2.5), respectively.

In principle, the vacuum energy density Λ could be set to zero by a judicious choice of renormalization scheme. However, since we will perform our calculations in a preset minimal subtraction scheme such as $\overline{\text{MS}}$, we do not have the freedom to set it to zero. Namely, the vacuum energy density is proportional to the gluon condensate, $\Lambda = \frac{d-4}{4d} \langle \frac{1}{g_s^2} F^2 \rangle$, which was estimated in [26, 27] using a combination of lattice and perturbative techniques. Its size however is of order $\sim (g_s^2 C_A)^3$ which is beyond the accuracy of our calculations and thus we can effectively ignore the second line of (2.10).

Beyond the decomposition into tensor structures, each two-point correlator is also decomposed into a loop-expansion

$$A_{\bullet} = \sum_{l=0} A_{\bullet}^{(l)} \quad (2.12)$$

where each $A_{\bullet}^{(l)}$ is proportional to the coupling $(g_s^2 C_A)^l$ and corresponds to the $L = l+1$ loop contribution to the two-point correlators. By dimensional analysis, the zeroth order terms come with a power $A_{\bullet} \propto p^d$ while each subsequent correction comes with an additional $1/p$ suppression at large momentum. The loop-expansion of the two-point functions is described explicitly to three-loops in sections 2.1 and 2.3.

Starting from four loops, the large- p expansion ceases to be perturbatively calculable due to the appearance of non-perturbative condensates. This can be understood by using the operator product expansion to separate calculable high-energy components from low-energy condensates (see [28]):

$$\int d^d x e^{ip \cdot x} \langle T^{\mu\nu}(x) T^{\alpha\beta}(0) \rangle_c \sim C_1^{\mu\nu\alpha\beta}(p) \langle \mathbb{1} \rangle + C_{F^2}^{\mu\nu\alpha\beta}(p) \langle \frac{1}{g_s^2} F^2(0) \rangle + \dots, \quad (2.13)$$

where it is easy to see from tree-level Wick contractions that $C_{F^2} \sim (p^2)^0 (g_s^2 C_A)^0$ while the corresponding expectation value is $\sim (g_s^2 C_A)^3$. The condensates will play no role in the present paper.

The structure of logarithms $\log(p^2)$ can be anticipated by applying the renormalization group equation (Callan-Symanzik equation) to (2.13) (see [29, 30]). The theory has a single coupling g_s^2 whose running, by dimensional analysis, cannot be affected by perturbative

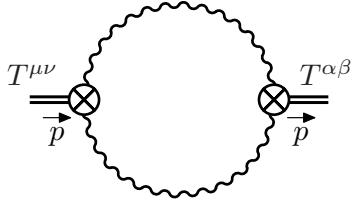


Figure 1: Feynman diagram for the 1-loop TT -correlation function. The circled cross denotes the vertex associated to the insertion of a stress-tensor.

quantum corrections at any order. The stress tensor $T^{\mu\nu}(x)$ does not renormalize multiplicatively. It mixes additively with $g^{\mu\nu}\mathbb{1}$ at four loops [31], but this does not affect the connected correlator (2.13). Thus the left-hand-side is independent of the $\overline{\text{MS}}$ scale $\bar{\mu}$ except for possible contact terms (polynomial in p), which can only appear at two and four loops by dimensional analysis, and can only affect specific combinations of A_0 , A_2 and Λ in accordance with (2.10). On the right-hand-side we can have mixing between the condensates, which again is only relevant starting from four loops. The most physically relevant combination, to be introduced in subsection 2.4, will turn out to cancel both two- and four-loop divergences.

2.1 One-loop two-point functions

In this section we present the one-loop two-point functions for $d = 3$. The generic d results can be found in appendix A.

The two-point functions (A_0 and A_2) were computed in generic dimension d using standard Feynman diagram techniques. We extract these two-point functions from the stress-tensor correlator using the tensor decomposition (2.10). This ensures that at each step we were working with Lorentz invariant quantities and is essential for the application of standard integration-by-parts (IBP) software such as FIRE [32].

In practice, we used Feynman rules in Feynman gauge. While gauge invariance of the two-point functions was not checked due to this choice, two other consistency checks were performed. First, the conservation of $\Pi^{\mu\nu\alpha\beta}$ was checked by contracting a factor of p into each hanging index of $\Pi^{\mu\nu\alpha\beta}$ while keeping the rest free. After applying IBP reduction, we find that the contraction of p with any index of $\Pi^{\mu\nu\alpha\beta}$ vanishes. Secondly, we cross-check the discontinuity of $\Pi^{\mu\nu\alpha\beta}$ in $d = 3$ at one- and two-loops from unitarity cuts.

At one-loop, there is a single Feynman diagram (see fig. 1) that contributes to the one-loop correlation function $\Pi^{\mu\nu\alpha\beta}$. The circled cross in figure 1 denotes the vertex associated to the stress-tensor coupling to two gluons which can be derived via standard textbook techniques [33–35]. After integral reduction and integration, the $d = 3$ two-point functions associated to the stress-tensor two-point function (2.10) are

$$A_0^{(0)}(p^2) \underset{d \rightarrow 3}{=} 2(p^2)^{3/2} + \mathcal{O}(\epsilon), \quad (2.14)$$

$$A_2^{(0)}(p^2) \underset{d \rightarrow 3}{=} (p^2)^{3/2} + \mathcal{O}(\epsilon). \quad (2.15)$$

2.2 One- and two-loop two-point functions via the unitarity method

In this section, we obtain the non-analytic part of the one-loop and two-loop correlation function, $\Pi^{\mu\nu\alpha\beta}$, with an independent calculation based on unitarity cuts.

We start by writing a general ansatz for the on-shell process of creating two gluons with momentum p_1 and p_2 from a stress-tensor operator $T^{\mu\nu}(p)$. Our ansatz needs to be a symmetric in p_1 and p_2 where the coefficients are fixed by imposing the conservation of the stress-tensor operator (i.e., $\partial_\mu T_{\mu\nu} = 0$). The form factor including the color factor is then,

$$\langle p_1^g p_2^g | T^{\mu\nu}(p) | 0 \rangle = \delta_{ab} (p_1^\mu p_2^\nu + p_1^\nu p_2^\mu - \delta^{\mu\nu} p_1 \cdot p_2). \quad (2.16)$$

To get the discontinuity of the one-loop correlation function depicted in figure 2, we cut the diagram and glue the two sides together using the Cutkosky cutting rules. This yields,

$$\begin{aligned} \text{Disc } \Pi^{\mu\nu\alpha\beta}(p^2) &= \frac{-id_G}{2!} \int \frac{d^2 p_1}{(2\pi)^2 2E_1} \frac{d^2 p_2}{(2\pi)^2 2E_2} (2\pi)^3 \delta^3(p - p_1 - p_2) \\ &\times \langle 0 | T^{\mu\nu}(p) | p_1^g p_2^g \rangle \langle p_1^g p_2^g | T^{\alpha\beta}(p) | 0 \rangle, \end{aligned} \quad (2.17)$$

where

$$\text{Disc } A(p^2) = A(p^2 - i\epsilon) - A(p^2 + i\epsilon). \quad (2.18)$$

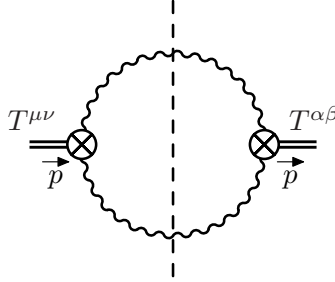


Figure 2: Cut of the 1-loop TT -correlation function is depicted. We can get each side (eq. (2.16)) from basic consistency principles (Bose symmetry and conservation of stress-tensor). We can then use unitarity cut to obtain the discontinuity of the correlation function.

Extracting the spin-0 and spin-2 two-point functions (see eq. (2.16)) and going to the rest frame of p ,

$$p = (\sqrt{s}, 0) \rightarrow \mathbf{p}_1 + \mathbf{p}_2 = 0, \quad E_1 + E_2 = \sqrt{s}, \quad (2.19)$$

the components of the correlation function (eq. (2.10)) are reduced to trivial integrals over the angles. For example,

$$\text{Disc } A_0^{(0)}(p^2) = \frac{-512i}{16\pi} \int d\theta \int \frac{dE_1}{E_1} \delta(\sqrt{s} - 2E_1) \frac{(2E_1^2)^2}{4} = \frac{4is^2}{\sqrt{s}}. \quad (2.20)$$

Using $\text{Disc}\sqrt{p^2} = -2i\sqrt{s}$, we can undo the cut to get the non-analytic contribution to the one-loop two-point function (2.10)

$$A_0^{(0)}(p^2) = 2(p^2)^{\frac{3}{2}}, \quad A_2^{(0)}(p^2) = (p^2)^{\frac{3}{2}}. \quad (2.21)$$

This, of course, matches eq. (2.14) when $d = 3$.

Next, we also compute the non-analytic part of the two-loop correlation function by employing unitarity cuts and on-shell form factors. This can then be compared with the full result including the analytic parts given in eq. (2.24).

We start by examining the unitarity cuts of the two-loop diagrams depicted in fig. 3. Importantly, the two-cuts of the double bubbles are complex conjugate to each other. This is because the tree-level form factor $\langle p_1^g p_2^g | T | 0 \rangle$ given by eq. (2.16) is real and goes as p^2 . Moreover, the one-loop form factor, which has an additional $g_s C_A$, must scale like $(p^2)^{1/2}$ and has a discontinuity that is purely imaginary. Thus, the double bubbles do not contribute to the discontinuity of the correlator since their imaginary part cancels when summed. This then means that the only contribution to the non-analytic part is contained in the right diagram in fig. 3.

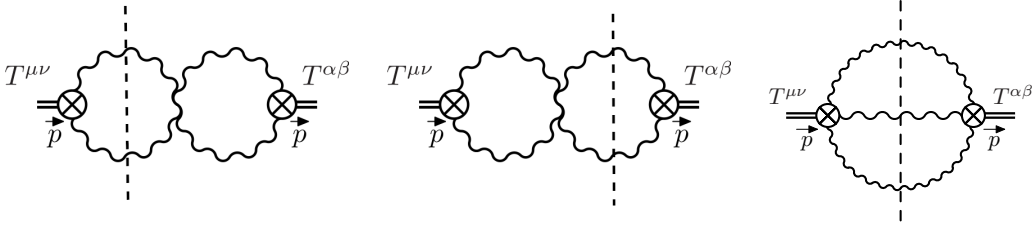


Figure 3: Unitarity cuts of the diagrams contributing to the two-loop stress-tensor two-point function. The first and second diagrams are complex conjugate of each other and once added have zero discontinuity. Only the third diagram contributes to the non-analytic part. The three-gluon form factor $\langle p_1^g p_2^g p_3^g | T^{\mu\nu} | 0 \rangle$ in the right most figure is calculated using BCFW recursion relation.

To calculate the unitarity cut in the right most diagram in fig. 3, we need the on-shell three-gluon form factor $\langle p_1^g p_2^g p_3^g | T^{\mu\nu} | 0 \rangle$. This is obtained by studying the four-dimensional two gluons form factor and then using BCFW [36, 37] as explained in appendix C.1. We can then go back to three-dimensions by using $\epsilon^{3d} = \frac{\epsilon^+ + \epsilon^-}{2}$ ². The final result for the three-gluon form factor is,

$$\langle p_1^g p_2^g p_3^g | T^{\mu\nu} | 0 \rangle = 2g_s f^{abc} \frac{\sum_{i=1}^3 (p_i^\mu p_i^\nu + p_i^\mu p_i^\nu - g^{\mu\nu} p_i \cdot p_i)(p_i \cdot p_i) - p_i^\mu p_i^\nu p_i^2}{\langle 12 \rangle \langle 23 \rangle \langle 31 \rangle}, \quad (2.22)$$

where $\langle 12 \rangle^2 = -2p_1 \cdot p_2$. As a consistency check, we have verified that this equation correctly reproduces the two-gluon form factor, $\langle p_1^g p_2^g | T^{\mu\nu} | 0 \rangle$, in the soft p_3 limit.

We then glue the form factors and perform the phase space integral as elucidated in appendix C.2 to obtain the non-analytic parts of the correlation function at 2-loops:

$$A_0^{(1)} = (g_s^2 C_A) \frac{8}{3\pi} p^2 \log(p^2), \quad A_2^{(1)} = -(g_s^2 C_A) \frac{8}{3\pi} p^2 \log p^2. \quad (2.23)$$

²This is because in three-dimensions the Lorentz group is isomorphic to $SU(2)$ whereas in four-dimension it is isomorphic to $SU(2) \times SU(2)$. Accordingly, the little group for massless particles changes from $SO(2)$ to Z_2

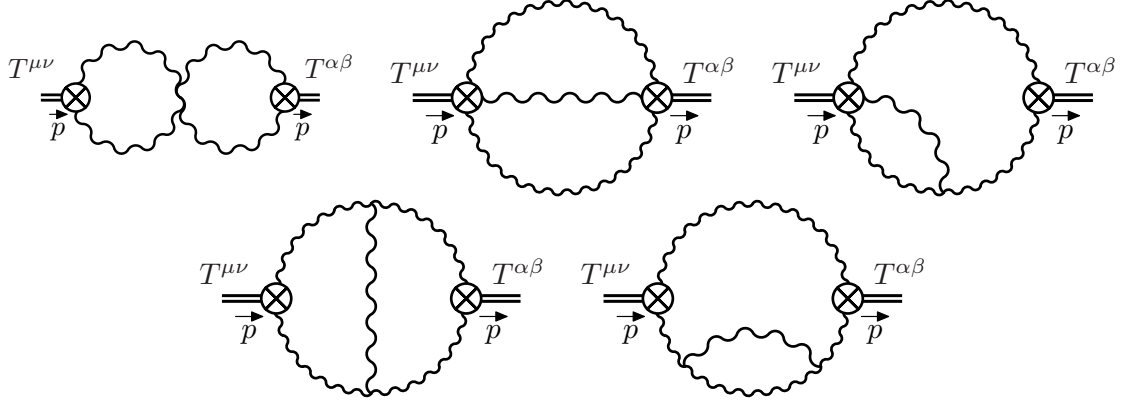


Figure 4: Feynman diagrams contributing to the two-loop stress-tensor two-point function. Note that there is another diagram not shown here where the gluon sub-bubble in the last diagram is replaced by a ghost bubble.

As expected, this correctly reproduces the non-analytic part of the stress-tensor two-point functions computed using Feynman diagram methods eq. (2.24) when $d = 3$. The fact that the scale dependence cancels when we sum these two channels will be significant below.

2.3 Two- and three-loop two-point functions

As we saw in the previous section, the unitarity method gives the imaginary part of the two-loop contribution to the stress-tensor two-point function (2.23). However, it will be useful to also have the constant part of the two-loop contribution since it contributes to the sum-rules. In fact, we do one-loop more and compute the stress-tensor two-point function to three-loops. Here, we will use Feynman diagrams because it is easier than d -dimensional unitarity. Since the calculation methodology was reviewed in section 2.1, we simply present the two- and three-loop two-point functions in this section

At two-loops the correlation function receives contributions from 8 diagrams including ghosts but only 7 topologies (see fig. 4). While there are 7 contributing topologies, there are only two scalar master integrals at two-loops (see equation (A.7) as well as equations (A.5) and (A.6)). When the dust settles, the two-loop $d = 3$ two-point functions are

$$A_0^{(1)}(p^2) \stackrel{d \rightarrow 3}{=} (g_s^2 C_A) p^2 \left[-\frac{1}{4} - \frac{4}{3\pi^2 \epsilon} + \frac{8}{3\pi^2} \log\left(\frac{p^2}{\bar{\mu}^2}\right) \right] + \mathcal{O}(\epsilon), \quad (2.24a)$$

$$A_2^{(1)}(p^2) \stackrel{d \rightarrow 3}{=} (g_s^2 C_A) p^2 \left[-1 + \frac{20}{3\pi^2} + \frac{4}{3\pi^2 \epsilon} - \frac{8}{3\pi^2} \log\left(\frac{p^2}{\bar{\mu}^2}\right) \right] + \mathcal{O}(\epsilon), \quad (2.24b)$$

where $\bar{\mu}^2 = 4\pi e^{-\gamma_E} \mu^2$ is the $\overline{\text{MS}}$ renormalization scale.

The three-loop correlation function receives contributions from a total of 41 different topologies where all consistent ways of distributing gluons and ghosts must be included. The three-loop parent topologies are listed in figure 5: all other topologies can be recovered from these by pinching a subset of propagators in a parent topology to points. Out of the 41 topologies, there are only 6 scalar master integrals (see equation (A.10)). The d -dimensional

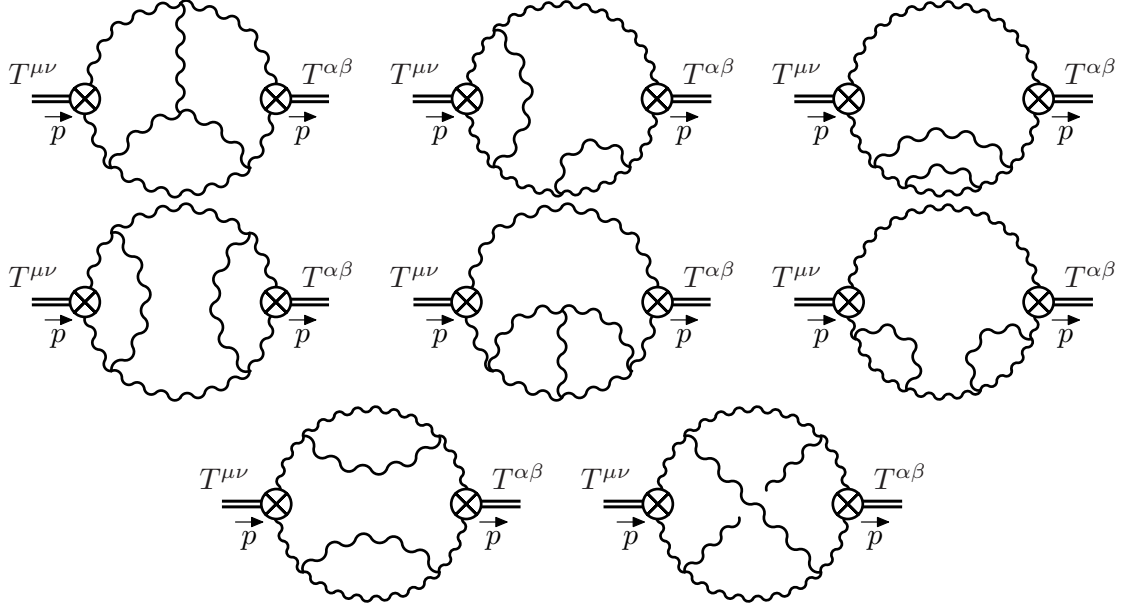


Figure 5: Parent topologies for all Feynman diagrams contributing to the three-loop stress-tensor two-point function. All other Feynman diagrams are pinches of these. All ghost contributions have been suppressed.

three-loop two-point functions are presented in equations (A.8) and (A.9). Taking the $d \rightarrow 3$ limit, we find

$$A_0^{(2)}(p^2) \underset{d \rightarrow 3}{=} (g_s^2 C_A)^2 \sqrt{p^2} \left[\frac{155}{384} - \frac{13}{2\pi^2} \right] + \mathcal{O}(\epsilon), \quad (2.25a)$$

$$A_2^{(2)}(p^2) \underset{d \rightarrow 3}{=} (g_s^2 C_A)^2 \sqrt{p^2} \left[\frac{431}{768} - \frac{37}{9\pi^2} \right] + \mathcal{O}(\epsilon). \quad (2.25b)$$

While most of the master integrals of (A.10) are easily evaluated, $I_1^{(3)}$ and $I_2^{(3)}$ are particularly challenging. Even though the ϵ -expansion of these integrals is known for $d = 4 - 2\epsilon$ [38–40], we had to recompute the generic d dependence from scratch in order to obtain the ϵ -expansion of these integrals in $d = 3 - 2\epsilon$. The generic d dependence of these integrals was determined using the method of dimensional recurrence and analyticity in d [41]. A summary of this method along with the equations needed to recover the d dependence of these integrals is presented in appendix B.

2.4 Superconvergent combination of two-point functions

In this section, we introduce a “superconvergent” combination of two-point functions A_0 and A_2 . This combination is exceptionally well behaved as $p^2 \rightarrow 0$, which we can use to ameliorate the convergence of the Källén-Lehmann representation. Thus, it is ideally suited for the application of dispersive sum-rules in section 3.

By expanding the tensor structure of the stress-tensor two-point function (2.10), one finds a term with four uncontracted momenta:

$$\Pi^{\mu\nu\alpha\beta}(p^2) = \mathcal{A}_{0+2}(p^2) p^\mu p^\nu p^\alpha p^\beta + \dots \quad (2.26)$$

where

$$\mathcal{A}_{0+2}(p^2) \equiv \frac{1}{(p^2)^2} \left(A_0(p^2) + \frac{2(d-2)}{(d-1)} A_2(p^2) \right). \quad (2.27)$$

Here, the change of calligraphy from A to \mathcal{A}_{0+2} highlights that a rescaling by $1/(p^2)^2$ has been applied. Since other terms in (2.26) are proportional to p^2 , the combination $\mathcal{A}_{0+2}(p^2)$ must be non-singular around $p^2 = 0$ in order for the correlator itself to be regular. However, thanks to the denominator in (2.27), it decays faster and in fact vanishes at infinite momenta. Thus, it satisfies an unsubtracted Källén-Lehmann dispersion relation.

By combining the one-loop (2.14), two-loop (2.25) and three-loop (2.25) results, we obtain the following perturbative result for the superconvergent two-point function \mathcal{A}_{0+2} in the three-dimensional limit:

$$\mathcal{A}_{0+2} = \frac{a_0}{\sqrt{p^2}} + a_1 \frac{g_s^2 C_A}{p^2} + a_2 \frac{(g_s^2 C_A)^2}{(p^2)^{3/2}} + a_3 \frac{(g_s^2 C_A)^3}{(p^2)^2} + \mathcal{O}\left(\frac{1}{(p^2)^{5/2}}\right). \quad (2.28)$$

Here,

$$a_0 = 3, \quad a_1 = \frac{16}{3\pi^2} - \frac{5}{4} \approx -0.710, \quad a_2 = \frac{247}{256} - \frac{191}{18\pi^2} \approx -0.110, \quad (2.29)$$

and C_A is the quadratic Casimir of the gauge group in the adjoint representation (i.e., $C_A = N_c$ for the gauge group $G = SU(N_c)$).

The superconvergent combination \mathcal{A}_{0+2} enjoys other nice properties. First, it is free from two-loop ultraviolet divergences, which can be checked explicitly by adding the two lines of (2.24). This is precisely as anticipated from the renormalization group argument below (2.13), since a two-loop divergence would have led to a non-polynomial term $\Pi^{\mu\nu\alpha\beta}(p) \sim \frac{p^\mu p^\nu p^\alpha p^\beta}{p^2} \log \bar{\mu}$. Thus, all constants in (2.29) are unambiguous and scheme-independent.

Second, even though we have not performed a four-loop calculation to determine a_3 , we can predict that this coefficient is actually independent of the gluon condensate, which cancels out in the combination \mathcal{A}_{0+2} . This can be seen from the fact that the Wick contraction of two field strengths that can give rise to the OPE coefficient $C_{F^2}^{\mu\nu\alpha\beta}$ in (2.13) following [30], cannot give rise to a $p^\mu p^\nu p^\alpha p^\beta$ term at leading order.³ Therefore, the perturbative calculation of a_3 cannot display any infrared sensitivity and so must yield a finite, unambiguous constant.

³Upon using the Ward identity (2.6) to fix all contact ambiguities and then imposing Lorentz invariance of condensates, we find specifically that

$$C_{F^2}^{\mu\nu\alpha\beta}(p) = \frac{d-4}{d} \left(\phi_0^{\mu\nu\alpha\beta}(p) \frac{2(d-2)}{(d-1)^2} + \phi_2^{\mu\nu\alpha\beta}(p) \frac{1}{d-1} + \frac{g^{\mu\alpha} g^{\nu\beta} + g^{\mu\beta} g^{\nu\alpha} - g^{\mu\nu} g^{\alpha\beta}}{4} \right) + \mathcal{O}(g_s^2/p), \quad (2.30)$$

which is compatible with (2.10) and the relation between the condensate and vacuum energy.

In eq. (2.28) we have still included the term a_3 to parameterize our ignorance of the four-loop physics. Given the decreasing pattern in the above coefficients, we believe that a reasonable range is for a_3 is

$$a_3 \in \left[-\frac{1}{10}, \frac{1}{10} \right] \quad (2.31)$$

so that $|a_3| < |a_2|$.

Further note that the result (2.28) is an asymptotic series in the large Euclidean region $p^2 \gg g_s^2 C_A$ and its apparent singularity at $p^2 = 0$ is an artifact of perturbation theory since \mathcal{A}_{0+2} must be regular at $p^2 = 0$ non-perturbatively.

3 Sum-rules: estimating the glueball masses and couplings

In this section, we review the dispersive sum-rules for the superconvergent combination \mathcal{A}_{0+2} . We start by constructing dispersion relations relating the TT -correlator in the Euclidean region to the correlator in the physical region in section 3.1. Then in section 3.2, we describe how the Borel transform improves the convergence of the perturbative series of \mathcal{A}_{0+2} in the limit $p^2 \rightarrow 0$. From the Borel transform of \mathcal{A}_{0+2} , we construct a function \hat{M}^2 that corresponds to the weighted average of the low-lying glueball masses. Then, we compare the \hat{M}^2 obtained from truncating the perturbative expression of \mathcal{A}_{0+2} to the \hat{M}^2 obtained from a non-perturbative model of \mathcal{A}_{0+2} . The Borel transform of the perturbative result for \mathcal{A}_{0+2} is given in section 3.3 while the Borel transform of the non-perturbative \mathcal{A}_{0+2} is given in section 3.4. In sections 3.5 and 3.6, we optimize the parameters of the one- and two-glueball models using a χ^2 fit and extract estimates for the low-lying glueball masses and their couplings to the stress-tensor. Lastly, in section 3.7, we compare our values obtained from sum-rules to the lattice results.

3.1 Dispersion relations

The superconvergent two-point function \mathcal{A}_{0+2} inherits a Källén-Lehmann representation

$$\mathcal{A}_{0+2}(p^2) = \frac{1}{\pi} \int_{\mathbb{R}^+} ds \frac{\rho(s)}{p^2 + s - i\epsilon} \quad (3.1)$$

from the two-point functions A_0 and A_2 (2.10).⁴ Here, ρ is called the spectral density and is positive for timelike momenta $q^2 = -s < 0$. The form of the spectral density follows directly from the spectral density of A_0 and A_2 ,

$$\rho(s) = \sum_{i=1}^n \frac{2\pi g_i^2}{(m_i^2)^2} \delta(s - m_i^2) + H(s) \Theta(s - s_0^2), \quad (3.2)$$

where m_i is the mass of the i^{th} bound state, g_i is the residue of the m_i pole (also the coupling constant of the i^{th} bound state) and the continuum is assumed to start at $s_0 \sim 4m_1^2$. Since the sum-rules are robust against perturbations in s_0 we set $s_0 = 4m_1^2$. The s -dependence of H is fixed by the asymptotic form of ρ , which is computable using perturbation theory.

⁴In general, the Fourier transform of any 2-point function always has a Källén-Lehmann representation.

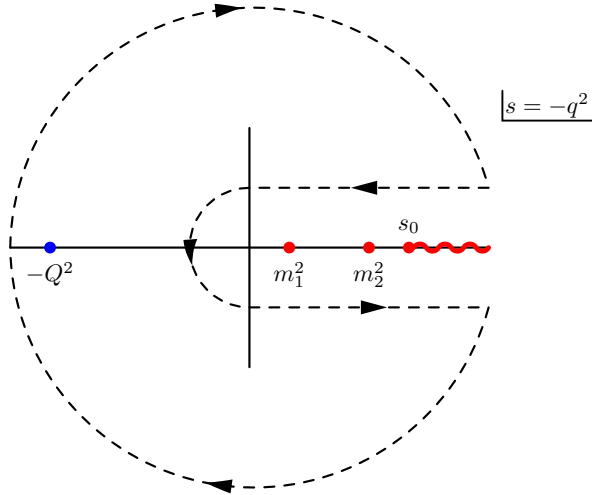


Figure 6: Analytic structure of \mathcal{A}_{0+2} , which follows from the Källén-Lehmann representation of A_{0+2} and the fact that $A_{0+2} \rightarrow 0$ faster than $(p^2)^2$ as $p^2 \rightarrow 0$. The minimal assumption is that there is a pole at $q^2 = -m_1^2$ associated to the spin-0 glueball then a branch cut that begins at $q^2 = s_0 \sim 4m_1^2$. Here, m_2 is the mass of the next bound state (spin-2 glueball), which may or may not lie below s_0 . The contour deformation used in the derivation of the dispersion relation is represented by the dashed line.

The normalization of the delta-function terms in (3.2) follows from the usual normalization of the A_0 and A_2 spectral densities and the fact that $\mathcal{A}_{0+2} = A_{0+2}/(p^2)^2$. The form of the spectral density determines the analytic structure of \mathcal{A}_{0+2} (see fig. 6).

While the two-point functions have been computed in the limit of large spacelike momenta $q^2 = Q^2 > 0$ (Euclidean region), we need \mathcal{A}_{0+2} in the region of large timelike momenta. Thankfully, these regions are linked by a dispersion relation. To see this, consider the following rewriting of \mathcal{A}_{0+2}

$$\mathcal{A}_{0+2}(Q^2) = \oint_{q^2=Q^2} \frac{dq^2}{2\pi i} \frac{\mathcal{A}_{0+2}(q^2)}{q^2 - Q^2}, \quad (3.3)$$

where the contour encircles the (spacelike) point Q^2 . Next, we deform the contour so that it encircles the poles along the real axis and hugs the branch cut in figure 6

$$\mathcal{A}_{0+2}(Q^2) = \int_0^\infty \frac{ds}{2\pi i} \frac{\text{Disc}\mathcal{A}_{0+2}(-s)}{s + Q^2} \quad (3.4)$$

where $\text{Disc}\mathcal{A}_{0+2}$ is the discontinuity of \mathcal{A}_{0+2} along the branch cut pictured in fig. 6

$$\text{Disc}\mathcal{A}_{0+2}(-s) = \mathcal{A}_{0+2}(-s - i\epsilon) - \mathcal{A}_{0+2}(-s + i\epsilon). \quad (3.5)$$

Comparing (3.1) and (3.4) we see that the spectral density is given by the discontinuity

$$\rho(s) = \frac{\text{Disc}\mathcal{A}_{0+2}(-s)}{2i}, \quad (3.6)$$

defined by the above contour deformation.

3.2 Borel transformation

The perturbative expansion of \mathcal{A}_{0+2} is an asymptotic series and thus cannot be extended to the region of small timelike momentum $s \sim 0$. Yet, in order to extract the mass of the low-energy bound states, we need to use the perturbative results at small s . To this end, we work with the Borel transform of \mathcal{A}_{0+2} , which improves the convergence of the asymptotic series and hope that the improved convergence of the perturbative result overlaps with low-energy glueball physics.

The Borel transformation of the superconvergent two-point function is

$$\hat{\mathcal{A}}_{0+2}(M^2) = \mathcal{B}_M \left[\frac{1}{\pi} \int ds \frac{\rho(s)}{s + Q^2} \right] = \frac{1}{\pi M^2} \int ds \rho(s) e^{-s/M^2}, \quad (3.7)$$

where M^2 is the Borel parameter [3]. A convenient way to implement the Borel transform of an asymptotic series in Euclidean momentum Q^2 is by acting with the following differential operator [3]

$$\mathcal{B}_M = \lim_{\substack{n \rightarrow \infty \\ Q^2 \rightarrow \infty \\ Q^2/n = M^2}} \frac{1}{(n-1)!} (Q^2)^n \left(-\frac{d}{dQ^2} \right)^n. \quad (3.8)$$

In particular, all polynomials in Q^2 are killed by the Borel transform and the following accounts for most applications

$$\mathcal{B}_M \left[\left(\frac{1}{Q^2} \right)^n \right] = \frac{1}{\Gamma(n) (M^2)^n}, \quad (3.9)$$

$$\mathcal{B}_M \left[\left(\frac{1}{Q^2} \right)^n \log Q^2 \right] = \frac{\log(M^2)}{\Gamma(n) (M^2)^n} + \frac{\Gamma'(n)}{\Gamma^2(n) (M^2)^n}, \quad (3.10)$$

In particular, note that the coefficient of $1/(Q^2)^n$ of the asymptotic series is suppressed by factor of $n!$ in the Borel transform

$$\mathcal{B}_M \left[\sum_{n \geq 0} a_n \frac{1}{(Q^2)^n} \right] = \sum_{n \geq 0} \frac{a_n}{n!} \frac{1}{(M^2)^n}. \quad (3.11)$$

The additional factors of $n!$ greatly improve the convergence of the Borel transformation for small Borel parameter M^2 . As a sanity check of (3.8), one can use the above to show that

$$\mathcal{B}_M \left[\frac{1}{s + Q^2} \right] = \frac{1}{M^2} e^{-s/M^2}. \quad (3.12)$$

Then, since $\mathcal{A}_{0+2}(Q^2)$ satisfies the dispersion relation (3.4), its Borel transform is exactly (3.7).

The Borel transform (3.7) allows us to define a weighted average of the mass

$$\hat{m}^2 \equiv \frac{\hat{\mathcal{A}}'_{0+2}(M^2)}{\hat{\mathcal{A}}_{0+2}(M^2)} = \frac{\int ds s \rho(s) e^{-s/M^2}}{\int ds \rho(s) e^{-s/M^2}} \quad (3.13)$$

where

$$\hat{\mathcal{A}}'_{0+2}(M^2) = -\frac{1}{M^2} \frac{\partial (M^2 \hat{\mathcal{A}}_{0+2})}{\partial (1/M^2)} = M^2 \frac{\partial (M^2 \hat{\mathcal{A}}_{0+2})}{\partial M^2} = \frac{1}{\pi M^2} \int ds s \rho(s) e^{-s/M^2}. \quad (3.14)$$

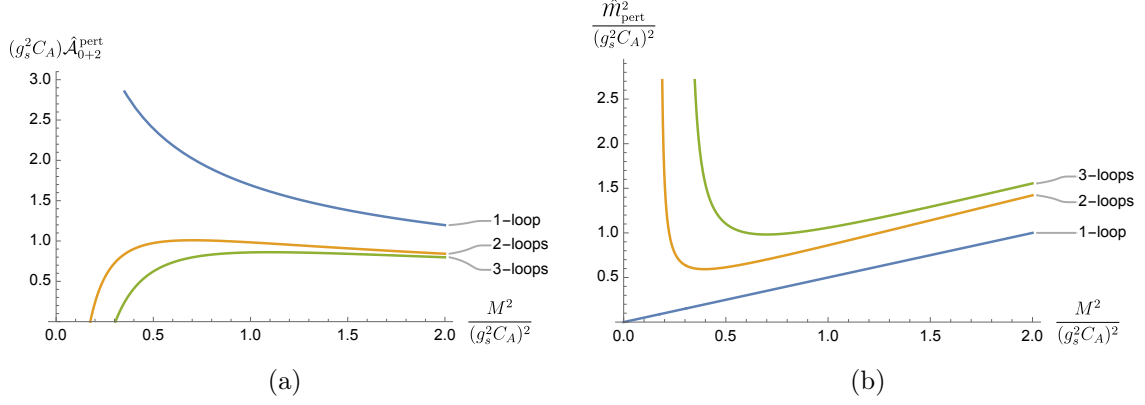


Figure 7: Figure 7a: The Borel transform of the superconvergent combination $\hat{\mathcal{A}}_{0+2}^{\text{pert}}$ at one-, two- and three-loops. The two- and three-loop curves converge quickly for $M^2 \gtrsim (g_s^2 C_A)^2/2$. Figure 7b: Weighted average of the mass (ratio of $\hat{\mathcal{A}}_{0+2}^{\text{pert}}$ and its weighted derivative). Note that at one-loop there is nothing stopping the mass from vanishing. On the other hand, the two- and three-loop curves turn up producing a minimum.

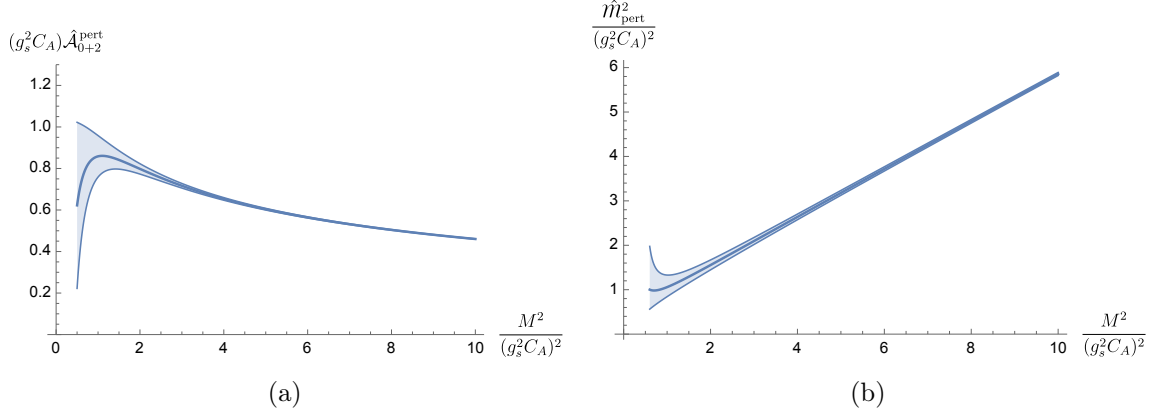


Figure 8: $\hat{\mathcal{A}}_{0+2}^{\text{pert}}$ and \hat{m}_{pert}^2 where the shaded region represent the error in our calculations due to the unknown four-loop contributions. The error is largest at low energy $M^2 \ll 1$ and shrinks to zero in the high energy limit $M^2 \gg 1$. These plots alone do not constrain the parameters of the one- and two-gluon models since the parameters can always be tuned such that both $\hat{\mathcal{A}}_{0+2}^{\text{non-pert}}$ and $\hat{m}_{\text{non-pert}}^2$ lie in the corresponding shaded region.

Provided that the spectral density ρ is dominated by the m_1 glueball, this quantity yields an estimate for m_1^2 . That is, at low M^2 , \hat{m}^2 should have a plateau at roughly the height m_1^2 . While this is indeed the case non-perturbatively, the truncated perturbative expression for \hat{m}^2 does not have this plateau due to the break-down of the perturbative series (as seen in figure 7b).

3.3 Borel transformation of the perturbative result

In this section, we compute the Borel transformation of the perturbative series of superconvergent two-point function. This will be used to estimate the mass and couplings of the

lightest glueball states in sections 3.5 and 3.6.

Using equations (3.9) and (3.10), we find that the Borel transform of the perturbative series for \mathcal{A}_{0+2} is

$$\begin{aligned}\hat{\mathcal{A}}_{0+2}^{\text{pert}}(M^2) &= \mathcal{B}_M [\text{three-loop truncation of } \mathcal{A}_{0+2}] \\ &= \frac{a_0}{\sqrt{\pi}\sqrt{M^2}} + a_1 \frac{g_s^2 C_A}{M^2} + \frac{2a_2 (g_s^2 C_A)^2}{\sqrt{\pi} (M^2)^{3/2}} + a_3 \frac{(g_s^2 C_A)^3}{(M^2)^2}.\end{aligned}\quad (3.15)$$

The one-, two- and three-loop Borel transforms of $\hat{\mathcal{A}}_{0+2}^{\text{pert}}$ are plotted in figure 7a. In particular, the two- and three-loop contributions converge very quickly for $M^2 \gtrsim g_s^2 C_A$ signaling that the three-loop curve can be trusted for $M^2 \gtrsim g_s^2 C_A$. However, it is uncertain how much we can trust the three-loop $\hat{\mathcal{A}}_{0+2}^{\text{pert}}$ for $M^2 < g_s^2 C_A$.

In order to try and quantify the uncertainty in $\hat{\mathcal{A}}_{0+2}^{\text{pert}}$, we have included an unknown “four-loop” term in $\mathcal{A}_{0+2}^{\text{pert}}$. The coefficient a_3 parameterizes the error in the perturbative result. We have set the magnitude of these coefficients to be approximately the same as as the three-loop correction to \mathcal{A}_{0+2} : $|a_3| < \frac{1}{10}$ (see figure 8a). In particular, note that the error band shrinks as $M^2 \rightarrow \infty$ where we are infinitely certain about the perturbative result but becomes very wide for small M^2 where we are the most uncertain of the perturbative result.

From equation (3.15), we compute the weighted mass average \hat{m}_{pert}^2

$$\frac{\hat{m}_{\text{pert}}^2}{(g_s^2 C_A)^2} = \frac{a_0 \frac{(M^2)^{3/2}}{(g_s^2 C_A)^3} - 2a_2 \frac{\sqrt{M^2}}{g_s^2 C_A} - 2\sqrt{\pi}a_3}{2a_0 \frac{(M^2)^{3/2}}{(g_s^2 C_A)^3} + 2\sqrt{\pi}a_1 \frac{M^2}{(g_s^2 C_A)^2} + 4a_2 \frac{\sqrt{M^2}}{g_s^2 C_A} + 2\sqrt{\pi}a_3}\quad (3.16)$$

Like $\hat{\mathcal{A}}_{0+2}^{\text{pert}}$, the two- and three-loop \hat{m}_{pert}^2 curves converge quickly for $M^2 \gtrsim g_s^2 C_A$ (see figure 7b). We can also plot a version of \hat{m}_{pert}^2 with an error band (see figure 8b).

3.4 Borel transformation of the non-perturbative model

In this section, we construct an ansatz/model for the non-perturbative spectral density of the superconvergent two-point function. From this spectral density, we construct a non-perturbative Borel transform of the superconvergent two-point function $\hat{\mathcal{A}}_{0+2}^{\text{non-pert}}$ and the analogous weighted mass average $\hat{m}_{\text{non-pert}}^2$. Like their perturbative cousins, these quantities will be used to estimate the mass and couplings of the lightest glueball states in sections 3.5 and 3.6.

We consider the following model of the non-perturbative spectral density

$$\rho(s) = \sum_{i=1}^N \frac{2\pi g_i^2}{m_i^4} \delta(s - m_i^2) + H(s) \Theta(s - 4m_1^2)\quad (3.17)$$

where $H(s)$ is fixed by the asymptotic behaviour of the perturbative spectral density

$$H(s) \equiv \text{Disc} \mathcal{A}_{0+2}^{\text{pert}}(-s) \Big|_{s > 4m_1^2} = \frac{a_0}{\sqrt{s}} + \frac{a_2 (g_s^2 C_A)^2}{s^{3/2}} + \mathcal{O}\left(\frac{1}{s^{5/2}}\right).\quad (3.18)$$

Note that this has the gross features expected non-perturbatively: a sum of delta functions for each glueball in the spectrum and a continuum that begins at the threshold of the lightest particle $s > 4m_1^2$.

Using (3.4), the Borel transform of $\mathcal{A}_{0+2}^{\text{non-pert}}$ is

$$\begin{aligned} \hat{\mathcal{A}}_{0+2}^{\text{non-pert}}(M^2) &= \sum_{i=1}^n \frac{2g_i^2}{M^2 m_i^4} e^{-\frac{m_i^2}{M^2}} + \frac{a_0}{\sqrt{\pi}\sqrt{M^2}} \operatorname{erfc}\left(\sqrt{\frac{4m_1^2}{M^2}}\right) \\ &+ \frac{g_s^2 C_A}{M^2} - \frac{a_2 g_s^2 C_A}{\pi m_1} e^{-\frac{4m_1^2}{M^2}} + \frac{2a_2 (g_s^2 C_A)^2}{\sqrt{\pi}(M^2)^{3/2}} \operatorname{erfc}\left(\sqrt{\frac{4m_1^2}{M^2}}\right) \end{aligned} \quad (3.19)$$

where $\operatorname{erfc}(z) = 1 - \operatorname{erf}(z)$ is the complimentary error function. We can fix one parameter in our model by comparing $\hat{\mathcal{A}}_{0+2}^{\text{pert}}$ and $\hat{\mathcal{A}}_{0+2}^{\text{non-pert}}$ in the large M^2 limit where we trust perturbation theory. Expanding in the large M^2 limit yields

$$\hat{\mathcal{A}}_{0+2}^{\text{non-pert}}(M^2) = \frac{a_0}{\sqrt{\pi}\sqrt{M^2}} + \frac{1}{\pi M^2} \left[\sum_{i=1}^n \frac{2\pi g_i^2}{m_i^4} - 4a_0 m_1 - a_2 \frac{(g_s^2 C_A)^2}{m_1} \right] + \mathcal{O}\left(\frac{1}{(M^2)^{3/2}}\right). \quad (3.20)$$

Then, requiring

$$[\hat{\mathcal{A}}_{0+2}^{\text{non-pert}}(M^2) - \hat{\mathcal{A}}_{0+2}^{\text{pert}}(M^2)]_{M^2 \rightarrow \infty} = \mathcal{O}\left(\frac{1}{(M^2)^{3/2}}\right), \quad (3.21)$$

fixes

$$g_1^2 = a_0 \frac{2m_1^5}{\pi} + a_1 \frac{(g_s^2 C_A)m_1^4}{2} + a_2 \frac{(g_s^2 C_A)^2 m_1^3}{2\pi} - \sum_{i=2}^n \frac{g_i^2 m_1^4}{m_i^4} \quad (3.22)$$

and guarantees that the high energy limit of $\hat{\mathcal{A}}_{0+2}^{\text{non-pert}}$ matches $\hat{\mathcal{A}}_{0+2}^{\text{pert}}$.

To fix the remaining parameters of the model, we minimize

$$\chi^2 = \sum_{j=0}^N \left(\frac{\hat{m}_{\text{pert}}^2(M_j^2)|_{a_3=0} - \hat{m}_{\text{non-pert}}^2(M_j^2)}{\operatorname{Error}(\hat{m}_{\text{pert}}^2(M_j^2))} \right)^2 \quad (3.23)$$

where $M_j^2 \in R_N$ and R_N is a region of Borel parameter space $R = M^2 \in [R_{\min}, R_{\max}]$ that has been discretized into $N + 1$ points. Since we know that the high energy limit of ρ is a power law, we want to sample the low energy region of \hat{m}^2 more frequently (by sampling the high energy region too much the fit can be driven to a pure power law that would only be accurate at high energies). Thus, R_N is logarithmically discretized

$$R_N \ni M_j^2 = \exp\left(\log R_{\min} + j \frac{\log R_{\max} - \log R_{\min}}{N}\right), \quad (3.24)$$

for $j = 0, 1, 2, \dots, N$.

3.5 One-globall model ($N = 1$)

In this section, we minimize (3.23) for a model with one-globall ($N = 1$ in (3.17)) and extract estimates for the mass m_1 and coupling g_1 .

The simplest model for the spectral density is the single globall model

$$\rho_1(s) = \frac{2\pi g_1^2}{m_1^4} \delta(s - m_1^2) + H(s) \Theta(s - 4m_1^2). \quad (3.25)$$

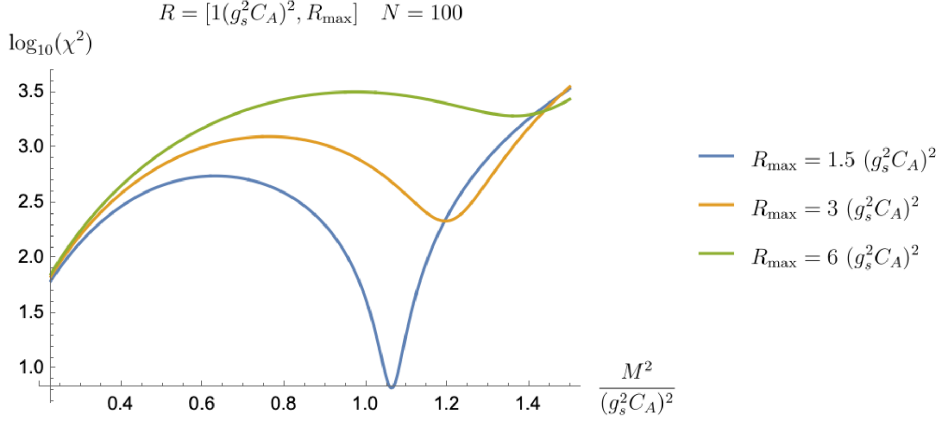


Figure 9: Plot of the 1-gluon $\log_{10}(\chi^2)$ for various choices of the fitting region R . The location of the minimum is very sensitive to the choice of R_{\max} . For “small” R_{\max} , the minimum is roughly at $m_1/(g_s^2 C_A) \sim 1$. After increasing R_{\max} sufficiently, what was a global minimum becomes a local minimum. For almost all choices of R_{\max} , the minimization of χ^2 puts too much emphasis on the high energy region. This stamps out the non-linearities in $\hat{m}_{\text{non-pert}}^2$ and drives to g_1^2 to zero which we deem unphysical.

The spin-0 glueball residue is fixed by (3.22) to

$$g_1^2 = \frac{247(g_s^2 C_A)^2 m_1^3}{512\pi} - \frac{191(g_s^2 C_A)^2 m_1^3}{36\pi^3} + \frac{8(g_s^2 C_A) m_1^4}{3\pi^2} - \frac{5(g_s^2 C_A) m_1^4}{8} + \frac{6m_1^5}{\pi}, \quad (3.26)$$

Moreover, since $m_1, g_1^2 > 0$, we obtain a lower bound on the spin-0 mass

$$\frac{m_1}{g_s^2 C_A} > m_{1,\min} \equiv \frac{\sqrt{79744 - 9069\pi^2 + 225\pi^4} + 15\pi^2 - 64}{288\pi} \approx 0.226377. \quad (3.27)$$

In the one-gluon model, the minimization of χ^2 is highly correlated to the selection of the region R . In figure 9, χ^2 is plotted as a function of the glueball mass m_1 for several choices of R . For small R_{\max} , the fit is trying to match the low energy regions best and there is a global minimum at $m_1 \sim 1.06(g_s^2 C_A)$. As R_{\max} is increased, what was the global minimum becomes a local minimum. The new global minimum forces m_1 to its minimal value (where $g_1^2 = 0$). By setting $g_1^2 = 0$, the fit wants to forget about the non-perturbative dynamics and instead match perturbation theory (figure 10b).

Given the sensitivity of the optimized m_1 on the choice of R_{\max} and the fact that using a low energy R_{\max} leads to a significant miss-match between \hat{m}_{pert}^2 and $\hat{m}_{\text{non-pert}}^2$ for $M^2 > 1$ (figure 10a), we conclude that the one-gluon model does not accurately describe the non-perturbative spectral density of \mathcal{A}_{0+2} .

3.6 Two-gluon model ($N = 2$)

Having concluded that the single gluon model does not accurately represent the non-perturbative spectral density of \mathcal{A}_{0+2} , we study the next simplest model containing two

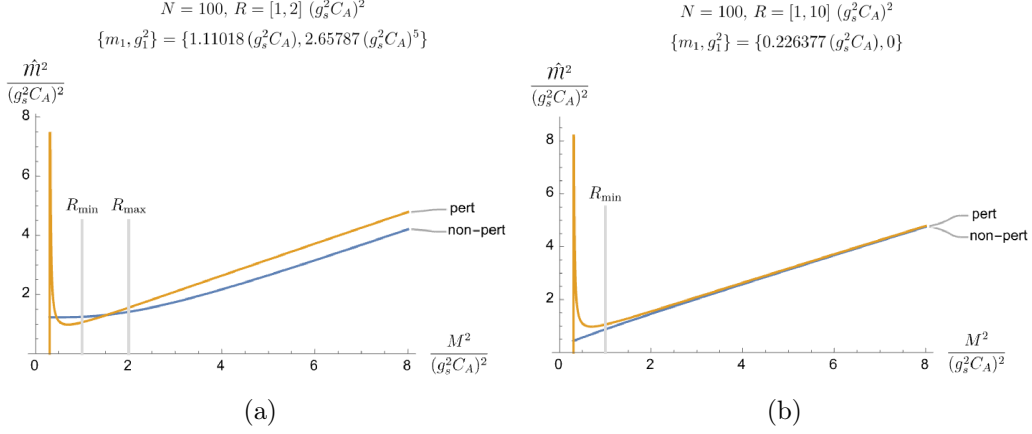


Figure 10: Plots of \hat{M}^2 (the ratio of $\hat{\mathcal{A}}_{0+2}$ and its derivative (3.13)) where the parameters have been optimized over different fitting regions R (indicated by the region between the grey vertical lines). In figure 10a the parameters have been optimized using a small R_{\max} . While m_1 is reasonable ($m_1/g_s^2 C_A \sim \mathcal{O}(1)$), there is still a sizable difference between $\hat{M}_{\text{non-pert}}^2$ and \hat{M}_{pert}^2 for $M^2 \geq 1$. In figure 10b the parameters have been optimized using a larger R_{\max} . Unsurprisingly, the high energy limit of $\hat{M}_{\text{non-pert}}^2$ fits \hat{M}_{pert}^2 better. By minimizing χ^2 over a larger region m_1 and g_1^2 are driven to their minimal values. Since \hat{M}_{pert}^2 is linear in the high energy region, the minimization sets $g_1^2 \rightarrow 0$ so that $\hat{M}_{\text{non-pert}}^2$ is as close to linear as possible. Given the sensitivity of the optimized parameters to the range R , the single glueball model is perhaps not the best.

glueballs. We will find that the optimized value for the masses and coupling of this model are much more stable.

Setting $N = 2$ in (3.17), the spectral density of the two glueball model is

$$\rho_2(s) = 2\pi \left[\frac{g_1^2}{m_1^2} \delta(s - m_1^2) + \frac{g_2^2}{m_2^2} \delta(s - m_2^2) \right] + H(s) \Theta(s - 4m_1^2). \quad (3.28)$$

By matching the asymptotics of $\mathcal{A}_{0+2}^{\text{pert}}$ and $\mathcal{A}_{0+2}^{\text{non-pert}}$, the coupling constant g_1^2 is fixed to

$$g_1^2 = -\frac{g_2^2 m_1^4}{m_2^4} + \frac{6m_1^5}{\pi} + \left(\frac{8}{3\pi^2} - \frac{5}{8} \right) m_1^4 (g_s^2 C_A) + \left(\frac{247}{512\pi} - \frac{191}{36\pi^3} \right) m_1^3 (g_s^2 C_A)^2. \quad (3.29)$$

Combining this with the constraints $m_i, g_i > 0$ and $m_{i+1} > m_i$, we find the same constraint on m_1 as for one glueball model

$$\frac{m_1}{g_s^2 C_A} > m_{1,\min} \approx 0.226377 \quad (3.30)$$

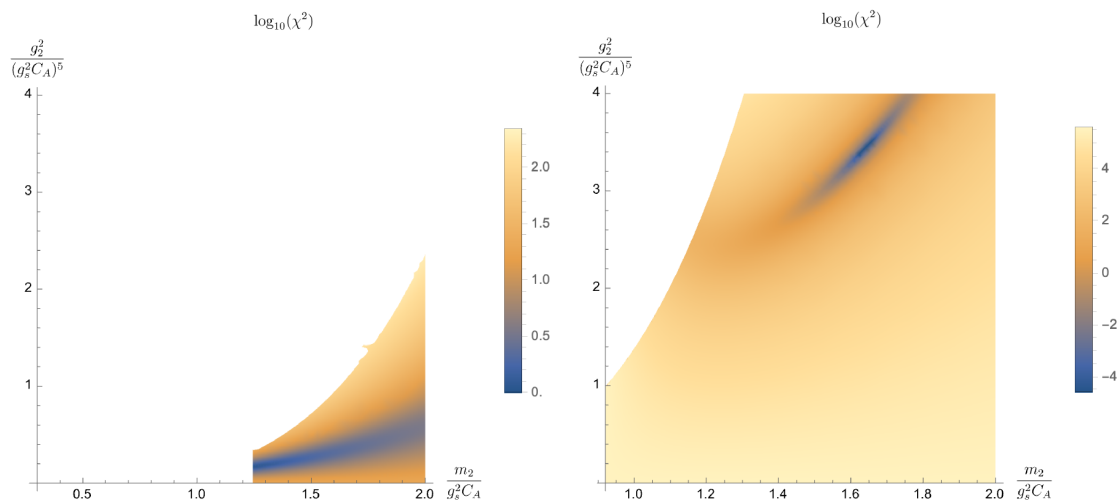
as well as a constraint on the coupling g_2^2

$$\frac{g_2^2}{(g_s^2 C_A)^5} < g_{2,\max}^2 \equiv \frac{6m_1 m_2^4}{\pi (g_s^2 C_A)^5} - \frac{(15\pi^2 - 64) m_2^4}{24\pi^2 (g_s^2 C_A)^4} + \frac{(2223\pi^2 - 24448) m_2^4}{4608\pi^3 (g_s^2 C_A)^3 m_1}. \quad (3.31)$$

Minimizing the two glueball χ^2 , we find estimates for the model parameters. In particular, the minimization of the two glueball χ^2 is robust to changes of the region R and the discretization parameter N :

N	$\frac{R_{\min}}{(g_s^2 C_A)^2}$	$\frac{R_{\max}}{(g_s^2 C_A)^2}$	$\frac{m_1}{g_s^2 C_A}$	$\frac{g_1^2}{(g_s^2 C_A)^5}$	$\frac{m_2}{g_s^2 C_A}$	$\frac{g_2^2}{(g_s^2 C_A)^5}$
10-100	1	10	0.93	0.69 \div 0.71	1.67 \div 1.68	3.64 \div 3.69
100	1-3	10	0.92 \div 0.93	0.65 \div 0.70	1.64 \div 1.67	3.46 \div 3.65
100	1	8-12	0.93	0.70	1.67	3.64 \div 3.67

We caution the reader that one has to (somewhat arbitrarily) decide on a reasonable range for the input parameters (N, R_{\min}, R_{\max}). While the estimates for m_1 and g_1^2 remain relatively stable, χ^2 is quite flat in the m_2 and g_2^2 directions. Thus, the m_2 and g_2^2 estimates are more sensitive to the choices of N, R_{\min} and R_{\max} . This will be more obvious in table 1 where we scan over values of the unknown four-loop contributions a_3 .



(a) Plot of $\log(\chi^2)$ at fixed $m_1/g_s^2 C_A = 0.30$. Here, we have chosen a value of m_1 that is close to its minimal value which places the global minimum of χ^2 outside of the allowed region. Note that while it is not shown at this scale, near the bottom axis the plot smoothly extends all the way to the left axis at $m_1 = m_{1,\min}$.

(b) Plot of $\log(\chi^2)$ at fixed $m_1/g_s^2 C_A = 0.92$. Here, we have chosen a value of m_1 that is close to its optimized value for which the global minimum of χ^2 lies inside the allowed region.

Figure 11: Density plots of $\log(\chi^2)$ at various values of m_1 in the allowed region (below equation 3.29).

Much like the one-gluon case, when R_{\min} is too large the minimization procedure puts too much emphasis on the high energy region and drives $m_1 \rightarrow m_{1,\min}$ as well as $g_1^2 \rightarrow 0$. In this case, the global minimum lies somewhere outside the allowed region in (m_2, g_2^2) -space (see figure 11a). However, for small enough R_{\min} , we get reasonable estimates for m_1 and g_2^2 where the global minimum is well inside the allowed region (see figure 11b).

Choosing the right R_{\min} is essential to extracting good estimates. This requires finding a window where one can still trust the extrapolation of perturbation theory and where the effects of the low-lying glueballs are significant. However, since we do not know exactly where

the perturbative expansion breaks down this choice can introduce significant error into our estimates. As a sanity check, we compare the relative strength of the continuum and glueball contributions to the Borel transform of the superconvergent two-point function in figure 12. For the optimized values of m_1, m_2, g_1^2 and g_2^2 , the relative strengths of the continuum and glueball contributions to the superconvergent combination align with physical expectations. Near the lowest lying glueball state, the contribution from the glueball dominates over the continuum. However, sometime after the first glueball but before the second glueball and threshold, the continuum starts to dominate. Moreover, the second glueball is subdominant in all regions and occurs below threshold. These properties are consistent with a physically reasonable spectral density and we are inclined to trust the optimized values of m_1, m_2, g_1^2 and g_2^2 . We also note that the ratio of the m_2 to m_1 contribution to $\hat{\mathcal{A}}_{0+2}^{\text{non-pert}}$ approaches 1/2 asymptotically. Since these contributions are asymptotically of the same order, this provides further evidence that the single glueball model (section 3.5) misses important effects. Roughly speaking, this means that perturbation theory is not any more sensitive to the m_1 glueball compared to the m_2 glueball.

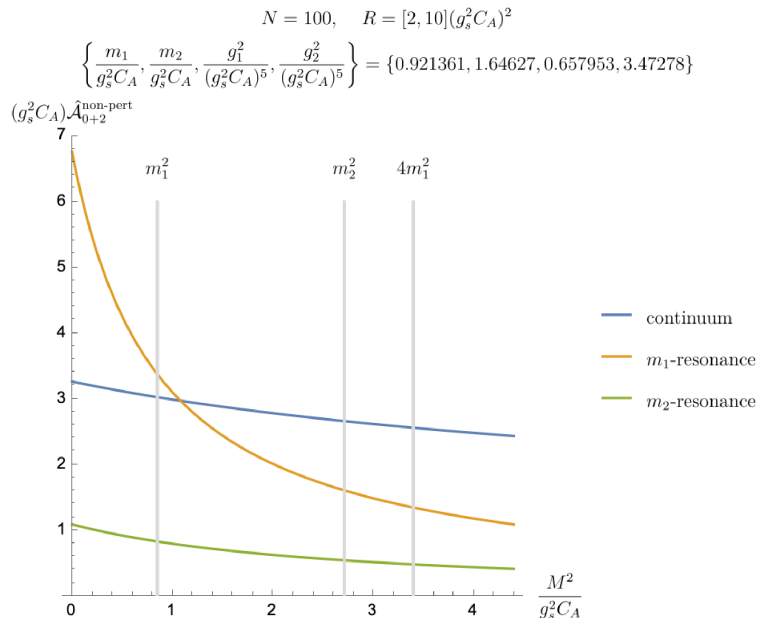


Figure 12: Plotting the individual contributions to the Borel transform of the superconvergent two-point function $\hat{\mathcal{A}}_{0+2}^{\text{non-pert}}$. This plot illustrates the relative strength of the threshold and glueball contributions. As expected, the m_1 glueball dominates for small Borel parameter $M^2 \sim m_1^2$ while the threshold contribution dominates for large Borel parameter $M^2 > 4m_1^2$. The m_2 -glueball is always sub-dominant as physically expected. However, the ratio of the m_2 to m_1 contribution approaches 1/2 asymptotically.

On the other hand, the above analysis assumed that $a_3 = 0$ in $\mathcal{A}_{0+2}^{\text{pert}}$. It is important to understand to what degree the unknown coefficients a_3 can change the optimized results. To get a rough idea, we repeat the above analysis for fixed a_3 in table 1. The only formula that changes is (3.23). Since we are not parameterizing the error in a_3 , we replace

$\text{Error}(\hat{m}_{\text{pert}}^2(M_j^2)) \rightarrow \hat{m}_{\text{pert}}^2(M_j^2)$ in (3.23). From table 1, we see that our estimates are relatively insensitive to the unknown coefficient a_3 . In particular, the optimized values for the lowest-lying mass m_1 and its coupling to the stress-tensor g_1 are stable in the regions

$$\frac{m_1}{g_s^2 C_A} \in [0.92, 0.94] \quad \text{and} \quad \frac{g_1^2}{(g_s^2 C_A)^5} \in [0.66, 0.74]. \quad (3.32)$$

Perhaps the insensitivity to a_3 can be seen from the fact that $H(s)$ (see (3.18)) does not depend on a_3 . This means that a_3 does not appear in the equations for the non-perturbative superconvergent two-point function $\hat{\mathcal{A}}_{0+2}^{\text{non-pert}}$ (3.19) or the lowest-lying residue (3.22). The only place a_3 appears is in the perturbative result for the weighted mass $\hat{m}_{\text{non-pert}}^2$. Thus, a_3 enters into the χ^2 fit in a relatively simple way.

a_3	N	$\frac{R_{\min}}{g_s^2 C_A}$	$\frac{R_{\max}}{g_s^2 C_A}$	$\frac{m_1}{g_s^2 C_A}$	$\frac{g_1^2}{(g_s^2 C_A)^5}$	$\frac{m_2}{g_s^2 C_A}$	$\frac{g_2^2}{(g_s^2 C_A)^5}$
$\frac{1}{5}$	20-100	1-2	10-20	$0.92 \div 0.94$	$0.66 \div 0.74$	$1.64 \div 1.70$	$3.48 \div 3.87$
$\frac{1}{10}$	20-100	1-2	10-20	$0.92 \div 0.94$	$0.66 \div 0.74$	$1.65 \div 1.70$	$3.48 \div 3.87$
0	20-100	1-2	10-20	$0.92 \div 0.94$	$0.66 \div 0.74$	$1.65 \div 1.70$	$3.48 \div 3.87$
$-\frac{1}{10}$	20-100	1-2	10-20	$0.92 \div 0.94$	$0.66 \div 0.74$	$1.65 \div 1.70$	$3.48 \div 3.87$
$-\frac{1}{5}$	20-100	1-2	10-20	$0.92 \div 0.94$	$0.66 \div 0.74$	$1.65 \div 1.70$	$3.48 \div 3.89$

Table 1: Table displaying mass estimates for some compatible values of the error a_3 . The above table shows that our estimates do not strongly depend on a_3 . While we suspect that only $|a_3| < 1/10$ are physically reasonable values, we show results with a_3 outside this range.

3.7 Comparison with lattice data

In this section, we summarize the low energy spectrum of three-dimensional YM theory predicted by lattice simulations and compare with the results of section 3.6.

Roughly speaking, observables are computed in lattice simulations by directly performing the Feynman path integral over field configurations on a discretized spacetime (often done using Monte Carlo sampling). By calculating a given observable for many different lattice spacings, one can determine a best fit for the dependence on the lattice spacing. Then extrapolating this fit to the limit of vanishing lattice spacing yields observables in the continuum theory.

Fortunately, there is a lot of data from lattice simulations of three-dimensional YM [7–20]. In particular, the spectrum for gauge group $G = SU(N_c)$ has been computed in [8, 17] for various N_c . However, this data must be converted from units of the string tension σ , which is the most accurate measurement on the lattice, to units of $g_s^2 N_c$.

The string tension is computed from the energy of the lowest-lying state of a static quark anti-quark pair separated by a distance R . If our theory has linear confinement, this

N_c	$m_1/(g_s^2 N_c)$	J^{PC}	$m_2/(g_s^2 N_c)$	J^{PC}
2	0.79	0^{++}	1.15	0^{++*}
3	0.80	0^{++}	1.19	0^{++*}
4	0.80	0^{++}	1.22	0^{++*}
\vdots				
∞	0.81	0^{++}	1.24	0^{++*}

Table 2: The first two masses and states in the spectrum computed by lattice simulations [17]. Note that we have only included states with quantum numbers $J = C = +$ since the stress tensor has quantum numbers $J = C = +$. With this restriction the lowest lying states are always 0^{++} and its excited state 0^{++*} .

energy, $E_{\min}(R)$, provides a definition for the static quark potential as well as a definition for the string tension σ in the large R limit

$$E_{\min}(R) \equiv V_{q\bar{q}}(R) \underset{R \rightarrow \infty}{\simeq} \sigma R \quad (3.33)$$

For large R , this state should be thought of as static quarks attached by a confining flux tube of length R . Reference [17] provides the most recent fit of the string tension in (2+1)-dimensional Yang-Mills theory

$$\sqrt{\sigma} = \left(0.196573(81) - \frac{0.1162(9)}{N_c^2} \right) g_s^2 N_c. \quad (3.34)$$

The mass values in units of $g_s^2 N_c$ are summarized in table 2. Comparing with table 1, we see that the sum-rule estimates for m_1 are in good agreement with the lattice data with error between 14% and 19% for any value of N_c . While the error for the m_2 estimates can be much larger (up to $\sim 48\%$), this comparison reveals that sum-rules capture many gross features of the low-energy non-perturbative physics. The discrepancy with the lattice data is likely due to the inaccuracies in our model of the spectral density that includes only one or two glueball states and a perturbative continuum. Despite these discrepancies, we conclude that this model is still a relative good first approximation.

4 Everything is consistent with unitarity!

In this section, we study the compatibility of the residues, g_i^2 , of the non-perturbative superconvergent spectral density (3.17) with the principle of unitarity and the perturbative two-point function eq. (2.28). In particular, we consider the case of a single glueball with mass m_1 and multi-particle threshold starting at $4m_1^2$. If the physical spectral density is indeed dominated by lightest the spin-0 glueball, this model would be a good approximation. While we have already argued against this approximation and that one should include at least two glueball states, the single glueball model is more constrained and therefore more relevant for the consistency checks.

Recalling eq. (3.25), the spectral density for the single glueball model is

$$\rho(s) = \frac{2\pi g_1^2}{(m_1^2)^2} \delta(s - m_1^2) + H(s) \Theta(s - s_0^2). \quad (4.1)$$

Checking unitarity of the correlation function boils down to checking the positivity of this spectral density.

To impose positivity, we consider a coordinate transformation of the s -plane that maps the upper half-plane to the unit disk while moving the pole to the origin and the branch cut to the boundary of the unit disk (see [42, 43]):

$$s \rightarrow z = \frac{\sqrt{4m_1^2 - s} - \sqrt{3}m_1}{\sqrt{4m_1^2 - s} + \sqrt{3}m_1}. \quad (4.2)$$

Now, the series expansion around $z = 0$ is convergent with a finite radius of convergence. Specifically, the superconvergent combination, \mathcal{A}_{0+2} , becomes

$$\mathcal{A}_{0+2}(z) = \frac{-g_1^2}{12m_1^6 z} + \sum_{n=0}^{\infty} c_n z^n, \quad (4.3)$$

which can be truncated at some large but finite cutoff N . On the other hand, the perturbative expansion for large Euclidean momenta ($s < 0$) maps to an asymptotic expansion around $z = 1$. Comparison with the three-loop perturbative result fixes three of the c_i 's. Next, we impose positivity on the boundary of the unit disk in the z -plane

$$\rho(z) = \frac{-\pi g_1^2}{6m_1^6} \delta(z) + \sum_{n=0}^N c_n \text{Im}(z^n) \geq 0, \quad (4.4)$$

where $z = e^{i\theta}$ and $\theta \in (0, \pi)$. In practice, we truncate the sum (4.4) at $N = 40$ and impose positivity for 2000 evenly-spaced points on the boundary of the disc. Using simple Mathematica functions (`FindMinimum` and `FindMaximum`), we minimize/maximize the residue g_1^2 over the variables $c_{i=4, \dots, 40}$ while enforcing the positivity condition (4.4) at the boundary points.⁵

Unfortunately, positivity of the physical cut alone is not enough to get a finite upper bound for the residue since both terms in (4.4) can be arbitrarily large positive numbers. We illustrate this in figure 13 (right) where we plot a positive spectral density with large residue $g_1^2 = 10^6 (g_s^2 C_A)^5$ and mass $m_1/g_s^2 C_A = 1$.

On the other hand, positivity only yields a trivial lower-bound for the residue. The minimization procedure returns negative values for the residue and adding more terms to the ansatz only increases the negativity of the residue. However, since the residue must be positive, we conclude that the minimal value of the residue must be zero. In figure 13 (left), we plot a positive spectral density with a small residue $g_1^2 = 10^{-6} (g_s^2 C_A)^5$ and mass $m_1/g_s^2 C_A = 1$ that is consistent with unitarity and the perturbative results.

⁵We have checked that the numerical solutions to the c_i are stable when we change the number of boundary points.

In this section, we solved the minimization/maximization problem of the residue g_1^2 for a wide range of mass values. For each mass, we find a spectral density that is compatible with unitarity and the asymptotics predicted by perturbation theory. Hence, we conclude that one can construct a spectral density compatible with unitarity and perturbation theory for any mass and residue in the single glueball model.

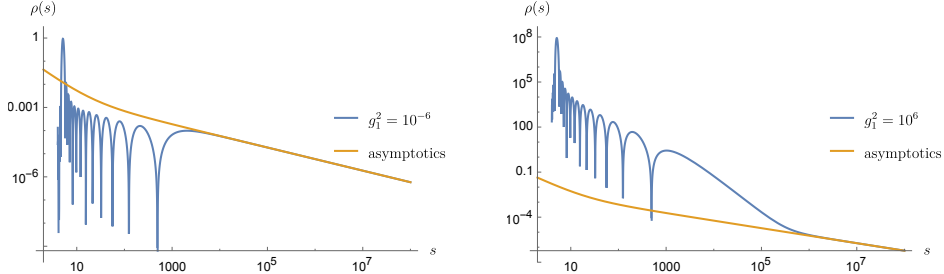


Figure 13: Log-log plot of the spectral density (4.4) at $m_1/(g_s^2 C_A) = 1$ as well as the asymptotic behaviour obtained from the perturbative loop expansion (equation (2.28)). For the spectral density (4.4), we set $N = 40$. The left plot corresponds to a spectral density with a large value of residue ($g_1^2 = 10^6 (g_s^2 C_A)^5$) and the right plot corresponds to a one with small value of residue ($g_1^2 = 10^{-6} (g_s^2 C_A)^5$). This exemplifies the argument that unitarity and the asymptotic behaviour of the correlation function are not strong enough to give an upper bound on the residue.

5 Higher-spin currents

In this section, we extend our analysis to more general operators, *i.e.*, higher-spin currents $O^{\mu_1 \dots \mu_\ell}(p)$ with even spin ℓ . As pointed out in the introduction, correlation functions of such operators contain important information about glueball lightcone wavefunctions, which are closely related to parton distribution functions. However, to apply the methods of section 3, we first need to identify superconvergent combinations of the higher-spin two-point functions.

In section 5.1, we analyze the tensor structure of higher-spin two-point functions of interest. Then, we fix a basis of the higher-spin operators in section 5.2. The coefficients of the tensor structures for the basis operators are then computed to two-loops. In section 5.3, we compute the imaginary part of these tensor structure coefficients using unitarity cuts at one- and two-loops. While just the imaginary parts are enough to verify the existence of superconvergent combinations, we also compute these coefficients using Feynman diagrams (section 5.4) since the sum-rules are sensitive to more than just the imaginary parts. Lastly, in section 5.5, we explicitly show the existence of superconvergent combinations for higher-spin two-point functions and give a crude method for extracting the higher-spin residues.

5.1 Higher-spin Correlation Functions

We start our analysis of higher-spin operators by noting that higher-spin fields can be defined as traceless symmetric combinations of covariant derivatives acting on the field strength $F_{\mu\nu}^a$.

In contrary to $T_{\mu\nu}$, these operators are not conserved and will have many more possible tensor structures.

At spin-2, there is only one operator: the stress-tensor. Explicitly,

$$O_2^{\mu_1\mu_2}(x) = (F^a)_{\lambda}^{\mu_1}(F^a)^{\mu_2\lambda} - \frac{g^{\mu_1\mu_2}}{d}(F^a)_{\mu\lambda}(F^a)^{\mu\lambda}. \quad (5.1)$$

For higher-spin operators with spin ℓ , there are $\ell/2$ possible structures:

$$\begin{aligned} O_{0,\ell}^{\mu_1\dots\mu_\ell}(x) &= \frac{1}{(\ell-2)!} [D^{(\mu_1} \dots D^{\mu_{\frac{\ell}{2}-1}} (F^a)_{\lambda}^{\mu_{\frac{\ell}{2}}} D^{\mu_{\frac{\ell}{2}+1}} \dots D^{\mu_{\ell-1}} (F^a)^{\mu_\ell)\lambda} - \text{trace}], \\ O_{i,\ell}^{\mu_1\dots\mu_\ell}(x) &= D^{\mu_1} \dots D^{\mu_i} O_{0,\ell-i}^{\mu_{i+1}\dots\mu_\ell} \quad \text{for } i = 2, \dots, \ell-2. \end{aligned} \quad (5.2)$$

Since we are interested in even spin operators, ℓ and i are even numbers. Any combination of these $\ell/2$ structures is a viable option for higher-spin operators. Later, we will introduce the criterion we use to select our basis of spin- ℓ operators.

To avoid working with indices, we utilize null vector representation for symmetric traceless tensor of spinning states, where we introduce $d+1$ -dimensional null vectors v with $v^2 = 0$,

$$f_{\mu_1\dots\mu_\ell} \leftrightarrow f(v) \equiv f_{\mu_1\dots\mu_\ell} v^{\mu_1} \dots v^{\mu_\ell}. \quad (5.3)$$

$f(v)$ can then be proved to be a harmonic polynomial of its d variable [44]. Once we have the function $f(v)$, we can reconstruct $f_{\mu_1\dots\mu_\ell}$ using Thomas-Todorov operator (see [44]):

$$D_v^\mu = \left(\frac{d}{2} - 1 + v \cdot \frac{\partial}{\partial v} \right) \frac{\partial}{\partial v_\mu} - \frac{1}{2} v^\mu \frac{\partial^2}{\partial v \cdot \partial v}. \quad (5.4)$$

This differential operator imposes tracelessness directly by removing the trace.

Since our goal is to study $\langle O_\ell(v_1, p) O_{\ell'}(v_2, -p) \rangle$ correlation functions, we need to understand how to extract different tensor structures. Because the correlation function must be invariant under little group transformations (transformations that keep the momentum, p , fixed), $O_\ell(p)$ and $O_{\ell'}(-p)$ must have opposite helicity under rotation around the p -axis. This means that the correlation function can be written as a sum over expressions with fixed helicity, j , under these rotations. The helicity j is an integer between 0 and $j_{\max} = \min(\ell, \ell')$. It is thus useful to define vectors that parameterize the directions perpendicular to p :

$$(v_i^\perp)^\mu = v_i^\mu - \frac{v_i \cdot p}{p^2} p^\mu. \quad (5.5)$$

These vectors are orthogonal to p and transform nicely under the little group. Along with p^μ , these vectors span all possible tensor structures. Thus, the correlation function can then be represented as,

$$\begin{aligned} \langle O_\ell(v_1, p) O_{\ell'}(v_2, -p) \rangle &= \sum_{j=0}^{\min(\ell, \ell')} [\pi_j]_{\ell, \ell'}(v, v', p) A_j^{\ell, \ell'}(p), \\ [\pi_j]_{\ell, \ell'}(v, v', p) &= (v_1^\perp \cdot v_1^\perp)^{\frac{\ell}{2}} (v_2^\perp \cdot v_2^\perp)^{\frac{\ell'}{2}} T_j(\cos \theta), \end{aligned} \quad (5.6)$$

where

$$\cos \theta = \frac{v_1^\perp \cdot v_2^\perp}{|v_1^\perp| |v_2^\perp|}. \quad (5.7)$$

Each helicity j structure in this expansion corresponds to a channel of spin j states in the Källén-Lehmann spectral decomposition of the correlator since it has the correct transformation under the little group.

5.2 Basis for higher-spin Operators

In this section, we define a “nice” basis for the operators (eqs. (5.1) and (5.2)).

To find this basis, we first write the on-shell matrix elements $\langle p_1^g p_2^g | O_{i,\ell} | 0 \rangle$ corresponding to these operators,

$$\begin{aligned} \langle p_1^g p_2^g | O_2 | 0 \rangle &= 2(v \cdot p_1)(v \cdot p_2) \delta^{a_1 a_2}, \\ \langle p_1^g p_2^g | O_{i,\ell} | 0 \rangle &= 2((v \cdot p_1) + (v \cdot p_2))^i ((v \cdot p_1)(v \cdot p_2))^{\frac{\ell-i}{2}}. \end{aligned} \quad (5.8)$$

There is a nice way of presenting these spin ℓ structures by introducing the angle ϕ via,

$$\cos \phi = \frac{v^\perp \cdot p_1^\perp}{|v^\perp| |p_1^\perp|} = \frac{v \cdot (p_1 - p_2)}{(v \cdot p)}. \quad (5.9)$$

In terms of this angle, the structures of eq. (5.8) simplify to:

$$\langle p_1^g p_2^g | O_{i,\ell} | 0 \rangle = 2^{i-\ell+1} (v \cdot p)^\ell \sin^{\ell-i} \phi. \quad (5.10)$$

We can then understand the decomposition of each of these two-point functions in the helicity basis $e^{ij\phi}$ using Chebyshev polynomials as a basis⁶:

$$\sin^{2n} \phi = -\frac{1}{\sqrt{\pi}} \frac{\Gamma(\frac{1}{2} + n)}{\Gamma(n+1)} + 2^{1-2n} \sum_{j=0}^n (-1)^j \binom{2n}{n-j} T_{2j}(\cos \phi). \quad (5.11)$$

We see that each of the form factors $\langle p_1^g p_2^g | O_{i,\ell} | 0 \rangle$ have all even helicities from 0 to ℓ . However, we can construct linear combinations of the $O_{i,\ell}$ operators such that the combinations only include helicity ℓ , $-\ell$ and 0:

$$\langle p_1^g p_2^g | \mathcal{Q}_\ell(p, v) | 0 \rangle = \delta^{ab} (-1)^{\frac{\ell}{2}} 2^{-2} (v \cdot p)^\ell (T_\ell(\cos \phi) - 1). \quad (5.12)$$

From this equation it is easy to read the relations between \mathcal{Q}_ℓ and $O_{i,\ell}$,

$$\mathcal{Q}_\ell = \sum_{m=0}^{\ell/2} \sum_{k=0}^{\frac{\ell-2m}{2}} 2^{2m+2k-1} \binom{\ell}{2m} \binom{\frac{\ell-2m}{2}}{k} (-1)^{\frac{\ell+2k+2m}{2}} O_{\ell-2m-2k,\ell} + \frac{(-1)^{\frac{\ell}{2}+1}}{8} O_{\ell,\ell}. \quad (5.13)$$

For instance for \mathcal{Q}_4 we have,

$$\mathcal{Q}_4 = 2^4 \left(O_{0,4} - \frac{1}{4} O_{2,4} \right). \quad (5.14)$$

This choice of basis then means that at one-loop we get:

$$\langle \mathcal{Q}_\ell \mathcal{Q}_{\ell'} \rangle = \frac{d_G}{512} \left(\pi_0 A_0^{\ell,\ell'(0)}(p^2) + \delta_{\ell\ell'} \pi_\ell A_\ell^{\ell,\ell'(0)}(p^2) \right). \quad (5.15)$$

However, note that at higher loops, all other projection channels appear again.

⁶This is because glueball states with spin m would be states with helicity $e^{im\phi} = T_m(\cos \phi) + iU(\cos \phi)$ and $e^{-im\phi} = T_m(\cos \phi) - iU(\cos \phi)$

5.3 One- and two-loop with unitarity method

Here, we will illustrate how to use unitarity methods to calculate the imaginary part of one- and two-loop correlation functions of spin-2 and spin 4 operators following section 2.2.

For one-loop, the needed phase space integrals are:

$$\begin{aligned} \text{Disc}(\langle \mathcal{Q}_\ell \mathcal{Q}_{\ell'} \rangle) &= \frac{-id_G}{2!} (-1)^{\frac{\ell+\ell'}{2}} 2^{-\ell-\ell'} \int \frac{d^2 p_1}{(2\pi)^2 2E_1} \frac{d^2 p_2}{(2\pi)^2 2E_2} (2\pi)^3 \delta^3(p - p_1 - p_2) \\ &\quad \times (v_1 \cdot p)^\ell (T_\ell(\cos \phi_1) - 1) (v_2 \cdot p)^{\ell'} (T_{\ell'}(\cos \phi_2) - 1), \end{aligned} \quad (5.16)$$

where we have used eq. (5.12) for the form factors inside the integral. We can then perform the phase space integral as illustrated in section 2.2 to obtain the correlation functions of any spin ℓ and ℓ' . The coefficients are simple to obtain for general spins:

$$A_0^{\ell, \ell'(0)} = 2(p^2)^{\frac{\ell+\ell'-1}{2}} \quad A_\ell^{\ell, \ell'(0)} = (p^2)^{\frac{\ell+\ell'-1}{2}}. \quad (5.17)$$

For example, the matrix-valued correlator of spin-2 and spin-4 operators can be written as:

$$\left(\begin{array}{cc} (p^2)^{-2} \langle \mathcal{Q}_2 \mathcal{Q}_2 \rangle & (p^2)^{-3} \langle \mathcal{Q}_2 \mathcal{Q}_4 \rangle \\ (p^2)^{-3} \langle \mathcal{Q}_4 \mathcal{Q}_2 \rangle & (p^2)^{-4} \langle \mathcal{Q}_4 \mathcal{Q}_4 \rangle \end{array} \right) \Big|_{1\text{-loop}} = \frac{d_G}{512\sqrt{p^2}} \left(\underbrace{\pi_0 \begin{pmatrix} 2 & 2 \\ 2 & 2 \end{pmatrix}}_{M_0^{(0)}} + \underbrace{\pi_2 \begin{pmatrix} 1 & 0 \\ 0 & 0 \end{pmatrix}}_{M_2^{(0)}} + \underbrace{\pi_4 \begin{pmatrix} 0 & 0 \\ 0 & 1 \end{pmatrix}}_{M_4^{(0)}} \right). \quad (5.18)$$

This takes care of one-loop analysis. Next, we examine these correlators at two-loops.

As discussed in section 2.2, the only ingredient we need is the on-shell form factor $\langle p_1^g p_2^g p_3^g | \mathcal{Q}_\ell | 0 \rangle$ as the other two cuts in fig. 3 cancel each other via the same argument presented in that section. To find this form factor, we use universality of the collinear and soft limit in the theory in addition to Bose symmetry. Basically, we first obtain the universal splitting factor appearing in the collinear limit by taking p_1 and p_2 to be parallel in the stress-tensor form factor $\langle p_1^g p_2^g p_3^g | \mathcal{T}^{\mu\nu} | 0 \rangle$ (eq. (2.22)) to compare with $\langle p_2^g p_3^g | \mathcal{T}^{\mu\nu} | 0 \rangle$ in eq. 2.16. This yields the following splitting factor:

$$\text{SP} = \frac{2g_s}{\sqrt{z(1-z)}\langle 12 \rangle} (1 - z + z^2). \quad (5.19)$$

Using this splitting factor, we obtain the three-gluon form factors:

$$\begin{aligned} \langle p_1^g p_2^g p_3^g | \mathcal{Q}_2 | 0 \rangle &= \frac{-16(p_1 \cdot v)^2 (p_2 \cdot p_3) + 8p^2 (p_1 \cdot v) (p_2 \cdot v) + 16(p_1 \cdot p_2) (v \cdot p_1) (p_1 \cdot p_2) + \text{perms}}{\langle 12 \rangle \langle 23 \rangle \langle 31 \rangle}, \\ \langle p_1^g p_2^g p_3^g | \mathcal{Q}_4 | 0 \rangle &= \frac{32\sqrt{2}}{\langle 12 \rangle \langle 23 \rangle \langle 31 \rangle} \left(-s_{23} (p_1 \cdot v)^4 + 2s_{12} (p_2 \cdot v) (p_1 \cdot v)^3 + s_{13} (p_2 \cdot v) (p_1 \cdot v)^3 \right. \\ &\quad \left. + 7s_{23} (p_2 \cdot v) (p_1 \cdot v)^3 - 4s_{12} (p_2 \cdot v)^2 (p_1 \cdot v)^2 - 7s_{13} (p_2 \cdot v)^2 (p_1 \cdot v)^2 - s_{12} \right. \\ &\quad \left. \times (p_2 \cdot v) (p_3 \cdot v) (p_1 \cdot v)^2 + 4s_{23} (p_2 \cdot v) (p_3 \cdot v) (p_1 \cdot v)^2 + \text{perms} \right). \end{aligned} \quad (5.20)$$

The three-gluon form factors are used to obtain the non-analytic part of two-loop correction to the correlation function of \mathcal{Q}_2 and \mathcal{Q}_4 through phase space integral explained in appendix C.2. We will postpone writing the explicit results of this calculation to the next section (eqs. (5.21) and 5.22) in which we do the one- and two-loop calculations using Feynman diagrams to obtain both analytic and non-analytic part.

5.4 Two-loop higher-spin correlators

Now that we fixed the basis for higher-spin operators, we use the Feynman diagram approach to obtain the two-loops contributions to the correlation functions of higher-spin operators.

The calculation is almost identical to that in section 5.4: one replaces the vertices associated to the stress-tensor with the vertices generated by equations (5.1), (5.2) and (5.14). Unlike in section 2 where we only had even spin structures, these higher-spin operators couple to both even and odd spin states.

The two-loop correction for the correlation functions \mathcal{Q}_2 and \mathcal{Q}_4 in eq. (5.18) are:

$$\left. \begin{pmatrix} (p^2)^{-2} \langle \mathcal{Q}_2 \mathcal{Q}_2 \rangle & (p^2)^{-3} \langle \mathcal{Q}_2 \mathcal{Q}_4 \rangle \\ (p^2)^{-3} \langle \mathcal{Q}_4 \mathcal{Q}_2 \rangle & (p^2)^{-4} \langle \mathcal{Q}_4 \mathcal{Q}_4 \rangle \end{pmatrix} \right|_{2\text{-loop}} = \frac{d_G g_s^2 C_A}{512 p^2} \left(\frac{\bar{\mu}^2}{p^2} \right)^{2\epsilon} \sum_{J=0}^4 \pi^J M_J^{(1)}, \quad (5.21)$$

where

$$\begin{aligned} M_0^{(1)} &= \begin{pmatrix} -\frac{1}{4} - \frac{4}{3\pi^2} - \frac{4}{3\pi^2\epsilon} & -\frac{1}{4} - \frac{272}{525\pi^2} - \frac{16}{15\pi^2\epsilon} \\ -\frac{1}{4} - \frac{272}{525\pi^2} - \frac{16}{15\pi^2\epsilon} & -\frac{1}{4} - \frac{14833664}{10735725\pi^2} - \frac{768}{715\pi^2\epsilon} \end{pmatrix}, \\ M_1^{(1)} &= \begin{pmatrix} 0 & 0 \\ 0 & -\frac{6903296}{32207175\pi^2} + \frac{3584}{6435\pi^2\epsilon} \end{pmatrix}, \\ M_2^{(1)} &= \begin{pmatrix} -1 + \frac{20}{3\pi^2} + \frac{4}{3\pi^2\epsilon} & -\frac{752}{255\pi^2} + \frac{16}{15\pi^2\epsilon} \\ -\frac{752}{255\pi^2} + \frac{16}{15\pi^2\epsilon} & -\frac{293698112}{19324305\pi^2} - \frac{448}{1287\pi^2\epsilon} \end{pmatrix}, \\ M_3^{(1)} &= \begin{pmatrix} 0 & 0 \\ 0 & -\frac{4632064}{5010005\pi^2} + \frac{1536}{1001\pi^2\epsilon} \end{pmatrix}, \\ M_4^{(1)} &= \begin{pmatrix} 0 & 0 \\ 0 & -2 + \frac{4487877952}{225450225\pi^2} + \frac{158272}{45045\pi^2\epsilon} \end{pmatrix}. \end{aligned} \quad (5.22)$$

We emphasize that the non-analytic part of (5.21) was cross-checked by a unitary computation.

5.5 Superconvergent Combinations

In section 2.4 we introduced the ‘‘superconvergent’’ combination for stress-tensor 2-point function which is well-behaved non-perturbatively in the $p^2 \rightarrow 0$ limit and well-suited for the application of dispersive sum-rules in section 3. In this section, we demonstrate the existence of such combinations for spinning correlation functions. We focus on the spin-2 and spin-4 operators for which we use the two-loop perturbative result obtained in previous subsection inside Borel sum-rules to extract crude estimates of their coupling to the lowest-lying spin 0 particle. This analysis is parallel to the analysis in section 3.5.

By following the argument in section 2.4, we see that the superconvergent combination for the correlator $\langle O_\ell O_{\ell'} \rangle$ is the coefficient of $p^{\mu_1} \dots p^{\mu_\ell} p^{\nu_1} \dots p^{\nu_{\ell'}}$. From eq. (5.6) it can be seen that this coefficient is given by:

$$\mathcal{A}_{\ell,\ell'}(p) = \sum_{j=0}^{\min(\ell,\ell')} T_j (-1)^j \frac{A_j^{\ell,\ell'}(p)}{(p^2)^{\frac{\ell+\ell'}{2}}} = \sum_{j=0}^{\min(\ell,\ell')} (-1)^j \frac{A_j^{\ell,\ell'}(p)}{(p^2)^{\frac{\ell+\ell'}{2}}}. \quad (5.23)$$

Thus, the resulting superconvergent version of the matrix $\langle \mathcal{Q}_\ell \mathcal{Q}_{\ell'} \rangle$ to two-loops in perturbation theory is

$$\begin{aligned} \begin{pmatrix} \mathcal{A}_{2,2}^{\text{pert}} & \mathcal{A}_{2,4}^{\text{pert}} \\ \mathcal{A}_{4,2}^{\text{pert}} & \mathcal{A}_{4,4}^{\text{pert}} \end{pmatrix} &= \begin{pmatrix} 3 & 2 \\ 2 & 3 \end{pmatrix} \frac{1}{\sqrt{p^2}} - \begin{pmatrix} \frac{5}{4} - \frac{16}{3\pi^2} & \frac{1}{4} + \frac{1216}{315\pi^2} \\ \frac{1}{4} + \frac{1216}{315\pi^2} & \frac{9}{4} - \frac{603392}{135135\pi^2} \end{pmatrix} \frac{g_s^2 C_A}{p^2} + \mathcal{O}\left(\frac{1}{(p^2)^{3/2}}\right), \\ &\approx \begin{pmatrix} 3 & 2 \\ 2 & 3 \end{pmatrix} \frac{1}{\sqrt{p^2}} - \begin{pmatrix} 0.710 & 0.641 \\ 0.641 & 1.798 \end{pmatrix} \frac{g_s^2 C_A}{p^2}. \end{aligned} \quad (5.24)$$

We see that in all of these equation the logarithms vanish, as anticipated. Like in section 3, the superconvergent two-point functions inherit a Källén-Lehmann spectral representation from the Källén-Lehmann representation of the $\langle \mathcal{Q}_\ell \mathcal{Q}_{\ell'} \rangle$:

$$\rho_{2,2}(s) = (3.17) = \sum_{i=1}^N \frac{2\pi g_i^2}{m_i^4} \delta(s - m_i^2) + H(s) \Theta(s - 4m_1^2), \quad (5.25)$$

$$\rho_{2,4}(s) = \sum_{i=1}^N \frac{2\pi g_{2,4;i}^2}{m_i^6} \delta(s - m_i^2) + H_{2,4}(s) \Theta(s - 4m_1^2), \quad (5.26)$$

$$\rho_{4,4}(s) = \sum_{i=1}^N \frac{2\pi g_{4,4;i}^2}{m_i^8} \delta(s - m_i^2) + H_{4,4}(s) \Theta(s - 4m_1^2), \quad (5.27)$$

where

$$H_{i,j}(s) = \text{Disc} \mathcal{A}_{i,j}^{\text{pert}}(-s) \Big|_{s > 4m_1^2}. \quad (5.28)$$

Note that due to contributions from odd-spin glueballs, the spectral density $\rho_{4,4}$ is not guaranteed to be positive. This is because odd-spin glueballs contribute with the wrong sign.

Requiring that the Borel transforms of $\mathcal{A}_{i,j}^{\text{pert}}$ and $\mathcal{A}_{i,j}^{\text{non-pert}}$ match asymptotically,

$$\left[\mathcal{A}_{i,j}^{\text{non-pert}}(M^2) - \mathcal{A}_{i,j}^{\text{pert}}(M^2) \right]_{M^2 \rightarrow \infty} = \mathcal{O}\left(\frac{1}{(M^2)^{3/2}}\right), \quad (5.29)$$

places constraints on the model parameters. Explicitly,

$$0 = 2 \sum_{i=1}^{\infty} \frac{g_i^2}{m_i^4} - \frac{12m_1}{\pi} + \left(\frac{15}{12} - \frac{16}{3\pi^2} \right) (g_s^2 C_A), \quad (5.30)$$

$$0 = 2 \sum_{i=1}^{\infty} \frac{g_{2,4;i}^2}{m_i^6} - \frac{8m_1}{\pi} + \left(\frac{1}{4} + \frac{1216}{315\pi^2} \right) (g_s^2 C_A), \quad (5.31)$$

$$0 = 2 \sum_{i=1}^{\infty} \frac{g_{4,4;i}^2}{m_i^8} - \frac{12m_1}{\pi} + \left(\frac{9}{4} - \frac{603392}{135135\pi^2} \right) (g_s^2 C_A). \quad (5.32)$$

For a very crude approximation of the residue g_1^2 , one can neglect all $g_{i>1}^2$ and solve the above equations for the coupling m_1 -coupling. Such an approximation is crude because as discovered in figure 12, the asymptotic contributions of the m_1 and m_2 glueballs are comparable. Thus, it is questionable as to whether we can neglect the m_2 glueball.

6 Conclusions

The basic idea of QCD sum-rules is the notion that the spectral density is well-approximated by a sum of delta-function(s) and a perturbatively calculable continuum. In this work, we have tested this notion for three-dimensional Yang-Mills theory.

In section 2, we calculated the stress-tensor two-point function to 3-loops ($\sim \alpha_s^2$) and extract a perturbative approximation to the spectral density above the continuum threshold (section 3) from the stress-tensor two-point function. Then, this is used to construct a model for the non-perturbative spectral density that, in turn, defines the non-perturbative stress-tensor two-point function. The masses and couplings (to the stress-tensor) of the first two glueballs in the spectrum were estimated by analyzing the Borel transformations of perturbative and non-perturbative stress-tensor two-point functions. While our estimates are not rigorous, there exists a reasonable range of parameters in the non-perturbative model where one finds stable results that are within 14 – 19% of the lattice data. Here, it was important to work with the Borel transformation of the two-point functions in order to improve the convergence of the perturbative expansion.

It was also crucial to combine the spin-0 and spin-2 parts (A_0 and A_2) of the stress-tensor two-point function into a “superconvergent” sum (2.27). Otherwise, we would have had to use a subtracted dispersion relation that removes the connection between the pole (glueball) and cut (continuum) contributions; the Borel transform of such a subtracted dispersion relation kills the first term in perturbation theory increasing the sensitivity to non-perturbative condensates. The existence of this superconvergent combination is tied to the spin of the stress tensor. For similar reasons, there also exists superconvergent dispersion relations for scattering amplitudes of spinning particles [45, 46].

In principle, it would be possible to extend our analysis of the stress-tensor correlator to four-loops since the non-perturbative condensate $\langle 0|F^2|0\rangle$ does not appear in the superconvergent combination. Even if the condensate did appear this would not necessarily be a showstopper since the $\overline{\text{MS}}$ condensate has been extracted from a combination of lattice and perturbative techniques [26, 27]. Furthermore, one could possibly bound the lattice regularized condensate using the bootstrap techniques of [47, 48].

We also showed that it is mathematically possible to find positive spectral densities that display the correct asymptotic behavior at large energies that are compatible with essentially any mass spectrum and residue strength (section 4). Finally, anticipating applications to higher moments of hadron wavefunctions (form factors of higher-spin lowest-twist operators), we also verified that superconvergent combinations of higher-spin operators exist (section 5). While we provide a crude method for approximating the higher-spin residues, we leave the analysis of higher-spin sum-rules to future work.

Our results in three-dimensional Yang-Mills theory adds numerical evidence to the effect that the Borel transform of perturbation theory can give a reasonable approximation to continuum spectral densities at finite energy, even when using a finite number of terms. This is similar to what has long been observed in the QCD context. Of course, it has never been clear how to rigorously justify this approximation and we do not claim to have ameliorated this state of affairs.

Acknowledgments

A.P. is grateful for support provided by the National Science and Engineering Council of Canada and the Fonds de Recherche du Québec — Nature et Technologies. A.P. is also supported by the Simons Investigator Award #376208 of A. Volovich. S.C.H.’s work is supported in parts by the National Science and Engineering Council of Canada (NSERC) and by the Canada Research Chair program, reference number CRC-2022-00421. S.C.H.’s work is additionally supported by a Simons Fellowships in Theoretical Physics and by the Simons Collaboration on the non-perturbative Bootstrap. Z.Z. is funded by Fonds de Recherche du Québec — Nature et Technologies, and the Simons Foundation through the Simons Collaboration on the non-perturbative Bootstrap. This project has received funding from the European Research Council (ERC) under the European Union’s Horizon 2020 research and innovation programme (grant agreement number 949077).

A d -dimensional form factors

In this appendix, we present the d -dimensional stress-tensor two-point functions up to three-loops. At three-loops, not all master integrals are known in closed form for generic d . However, once d is fixed these integrals can be computed via dimensional recursion [41].

A.1 One-loop

The one-loop two-point functions for generic dimension are

$$A_0^{(1)}(p^2; d) = \frac{512}{8(d-1)^2} \left[(d-4)^2(d-2)p^4 I_1^{(1)}(p^2; d) \right], \quad (\text{A.1})$$

$$A_2^{(1)}(p^2; d) = \frac{512}{8(d-1)(d+1)} \left[(2d^2 - 3d - 8)p^4 I_1^{(1)}(p^2; d) \right], \quad (\text{A.2})$$

where $I_1^{(1)}$ is the scalar bubble integral and the normalization is determined by equation (2.10). While the bubble integral is trivial, we quote it here so that our conventions are explicit

$$I_1^{(1)}(p^2; d) \equiv B_{1,1}(p^2; d) \quad (\text{A.3})$$

where

$$\begin{aligned} B_{a,b}(k^2; d) &= \int \frac{d^d \ell}{i(2\pi)^d} \frac{1}{[\ell^2]^a [(\ell+k)^2]^b} \\ &= \frac{1}{(4\pi)^{\frac{d}{2}}} \frac{\Gamma(a+b-\frac{d}{2}) \Gamma(\frac{d}{2}-a) \Gamma(\frac{d}{2}-b)}{\Gamma(a) \Gamma(b) \Gamma(d-a-b)} (k^2)^{\frac{d}{2}-(a+b)}. \end{aligned} \quad (\text{A.4})$$

With the exception of the three-loop master integrals $I_1^{(3)}$ and $I_2^{(3)}$, all other two- and three-loop master integrals can be computed in closed form from recursive use of (A.4).

A.2 Two-loops

The two-loop contributions to the stress-tensor two-point functions in generic dimension are

$$A_0^{(2)}(p^2; d) = \frac{512(g_s^2 C_A)}{8(d-1)^2} \left[(d-4)(d^3-16d^2+68d-88)p^4 I_1^{(2)}(p^2; d) - \frac{16}{3}(4d^3-33d^2+94d-92)p^2 I_2^{(2)}(p^2; d) \right] \quad (\text{A.5})$$

$$A_2^{(2)}(p^2; d) = -\frac{512(g_s^2 C_A)}{8(d-1)(d+1)} \left[\frac{8(d^4-8d^3+16d^2+20d-68)p^4}{(d-4)(d-2)} I_1^{(2)}(p^2; d) + \frac{8(13d^5-129d^4+462d^3-572d^2-376d+1088)p^2}{3(d-4)^2(d-2)} I_2^{(2)}(p^2; d) \right] \quad (\text{A.6})$$

where the master integrals are

$$I_1^{(2)}(p^2; d) = \frac{\text{---}}{\vec{p}} \text{---} \left(\text{---} \right) \text{---}, \quad I_2^{(2)}(p^2; d) = \frac{\text{---}}{\vec{p}} \text{---} \left(\text{---} \right) \text{---}. \quad (\text{A.7})$$

These master integrals are easily evaluated by repeated use of (A.4).

A.3 Three-loops

The three-loop contributions to the stress-tensor two-point functions in generic dimension are

$$A_0^{(3)}(p^2; d) = \frac{512(g_s^2 C_A)^2}{8(d-1)^2} \left[-\frac{3(d-4)^2(d-3)(d-2)(3d-8)p^8 I_1^{(3)}(p^2; d)}{4(2d-7)(2d-5)} - \frac{(d^3-16d^2+68d-88)^2 p^4 I_3^{(3)}(p^2; d)}{d-2} + (657d^7-11454d^6+85564d^5-354832d^4+880176d^3-1299616d^2 + 1048384d-350976) \frac{p^2 I_5^{(3)}(p^2; d)}{2(d-4)(d-2)(d-1)(2d-5)} - (108d^8-2661d^7+28822d^6-177546d^5+674735d^4-1607602d^3 + 2325996d^2-1848920d+607968) \frac{p^4 I_2^{(3)}(p^2; d)}{2(d-2)(d-1)(2d-7)(2d-5)} + (192d^{10}-6947d^9+105470d^8-907248d^7+4958664d^6-18113645d^5 + 44930982d^4-74791460d^3+79854504d^2-49204128d + 13194496) \frac{p^2 I_4^{(3)}(p^2; d)}{(d-4)(d-3)(d-2)(d-1)(2d-7)(2d-5)} + (162d^{11}-5487d^{10}+87553d^9-858385d^8+5673221d^7-26253008d^6 + 86068824d^5-198637272d^4+314636144d^3-324171296d^2 + 194410240d-50999296) \frac{I_6^{(3)}(p^2; d)}{(d-4)^2(d-3)^2(d-2)(d-1)(2d-7)} \right] \quad (\text{A.8})$$

and

$$\begin{aligned}
A_2^{(3)}(p^2; d) = & \frac{512(g_s^2 C_A)^2}{8(d-1)(d+1)} \left[-\frac{(16d^5 - 149d^4 + 397d^3 + 142d^2 - 1832d + 1696) p^8 I_1^{(3)}(p^2; d)}{4(d-2)(2d-7)(2d-5)} \right. \\
& - \frac{8(4d^8 - 62d^7 + 371d^6 - 939d^5 + 128d^4 + 4260d^3 - 7712d^2 + 3584d + 384) p^4 I_3^{(3)}(p^2; d)}{(d-4)^2(d-2)^2(d-1)d} \\
& + (1042d^{10} - 19207d^9 + 147122d^8 - 588708d^7 + 1199632d^6 - 543184d^5 - 3040032d^4 \\
& \left. + 7331904d^3 - 7007488d^2 + 2514944d + 24576) \frac{p^2 I_5^{(3)}(p^2; d)}{2(d-4)^3(d-2)^2(d-1)d(2d-5)} \right. \\
& - (1680d^{12} - 43447d^{11} + 499154d^{10} - 3324848d^9 + 13961672d^8 - 36985777d^7 \\
& + 54553314d^6 - 11375804d^5 - 120445352d^4 + 236351744d^3 - 195105152d^2 \\
& \left. + 60414976d + 1720320) \frac{p^2 I_4^{(3)}(p^2; d)}{(d-4)^3(d-3)(d-2)^2(d-1)d(2d-7)(2d-5)} \right. \\
& - (72d^{12} - 1812d^{11} + 24945d^{10} - 234230d^9 + 1498316d^8 - 6288301d^7 + 16330266d^6 \\
& - 22168812d^5 + 1696440d^4 + 41289728d^3 - 55822976d^2 + 25437184d - 1720320) \\
& \times \frac{p^4 I_2^{(3)}(p^2; d)}{2(d-4)^2(d-2)^2(d-1)d(2d-7)(2d-5)(3d-8)} \\
& - (432d^{15} - 27558d^{14} + 582633d^{13} - 6158463d^{12} + 35473743d^{11} - 89675899d^{10} \\
& - 197920872d^9 + 2586125488d^8 - 10618482072d^7 + 25226597520d^6 \\
& - 36849379104d^5 + 30607655680d^4 - 9263259648d^3 - 4995555328d^2 \\
& \left. + 3991977984d - 421134336) \frac{I_6^{(3)}(p^2; d)}{3(d-4)^4(d-3)^2(d-2)^2(d-1)d(2d-7)(3d-8)} \right] \quad (\text{A.9})
\end{aligned}$$

where

$$\begin{aligned}
I_1^{(3)}(p^2; d) &= \overrightarrow{p} \text{---} \langle \text{circle with } X \text{ inside} \rangle \text{---}, & I_2^{(3)}(p^2; d) &= \overrightarrow{p} \text{---} \langle \text{circle with two internal lines} \rangle \text{---}, \\
I_3^{(3)}(p^2; d) &= \overrightarrow{p} \text{---} \langle \text{three circles in a row} \rangle \text{---}, & I_4^{(3)}(p^2; d) &= \overrightarrow{p} \text{---} \langle \text{circle with two internal lines} \rangle \text{---}, \\
I_5^{(3)}(p^2; d) &= \overrightarrow{p} \text{---} \langle \text{two circles side-by-side} \rangle \text{---}, & I_6^{(3)}(p^2; d) &= \overrightarrow{p} \text{---} \langle \text{circle with two internal lines} \rangle \text{---}, \quad (\text{A.10})
\end{aligned}$$

are the scalar master integrals at three-loops. All but $I_1^{(3)}$ and $I_2^{(3)}$ are easily evaluated by repeated use of (A.4).

While ε -expansion of $I_1^{(3)}$ and $I_2^{(3)}$ are known near four-dimensions [38, 40], we must compute these expansions from scratch near three-dimensions since certain simplifications in four-dimensions are *not* present in three-dimensions. We use the method of dimensional recursion [41] (reviewed in appendix B) to find d -dimensional formulas for $I_1^{(3)}$ and $I_2^{(3)}$.

In three-dimensions, these integrals simplify to

$$\begin{aligned} I_1^{(3)}(p^2) &\underset{d \rightarrow 3}{=} -\frac{(2\pi^2 - 39)}{192\pi^2(p^2)^{7/2}}, \\ I_2^{(3)}(p^2) &\underset{d \rightarrow 3}{=} \frac{1}{512(p^2)^{3/2}}. \end{aligned} \tag{A.11}$$

Since the coefficients of $I_1^{(3)}$ and $I_2^{(3)}$ in equations (A.8) and (A.9) are finite in the limit $d \rightarrow 3$, the above formulas are sufficient for determining the three-loop contributions to A_0 and A_2 .

B Computing $I_1^{(3)}$ and $I_2^{(3)}$ from dimensional recurrence

In this appendix, we provide a short overview of the method of dimensional recurrence B.1 and provide formulas to compute $I_1^{(3)}$ and $I_2^{(3)}$ in any dimension (section B.2).

B.1 Dimensional recurrence and analyticity in d

In this short review of the method of dimensional recurrence and analyticity in d [41], we keep the discussion general. We specify to the integral family relevant to $I_1^{(3)}$ and $I_2^{(3)}$ in section B.2.

Suppose that we are given a family of Feynman integrals \mathbf{I} that is closed under IBP relations. Then, this family satisfies the following dimensional recurrence relation

$$\mathbf{I}(d+2) = \underline{\mathbf{R}}(d) \cdot \mathbf{I}(d). \tag{B.1}$$

Additionally, all Feynman integrals have the following projective parametric representation⁷

$$I = \int \left(\prod_{i=1}^L \frac{d^d \ell_i}{i(2\pi)^d} \right) \left(\prod_{j=1}^N \frac{1}{D_j^{n_j}} \right) = \Gamma(\omega) \int_{(\mathbb{R}^+)^N} d^N \mathbf{x} \left(\prod_{i=1}^N \frac{x_i^{n_i-1}}{\Gamma(n_i)} \right) \frac{\delta(1-h(\mathbf{x}))}{\mathcal{U}^{\frac{d}{2}-\omega} \mathcal{F}^\omega} \tag{B.2}$$

where $\omega(d) = \frac{d}{2} - |\mathbf{n}|$ is the superficial degree of divergence, x_i is the Schwinger parameter associated to the propagator D_j , $h(\mathbf{x})$ is any degree 1 homogeneous polynomial, and, \mathcal{U} and \mathcal{F} are the first and second Symanzik polynomials. Using the projective representation (B.2), one can bound the large imaginary d limit of a Feynman integral

$$|I(d)| \lesssim \text{const.} \times |\text{Im } d|^{\omega(\text{Re } d) - \frac{1}{2}} e^{-\frac{\pi}{4} L \text{Im } d}. \tag{B.3}$$

Then, using the above bound and provided that there exists a strip $S = \{d \in \mathbb{C} | d_{\min} < \text{Re } d < d_{\max}\}$ that is known to be free from poles, the homogenous solution to the recurrence relation (B.1) can be constructed.

⁷By projective, we mean that I is invariant under the rescaling of \mathbf{x} : $\mathbf{x} \rightarrow \lambda \mathbf{x}$.

The first step to solve the recurrence relation (B.1) is to define the so-called summing factors $\Sigma(d)$ such that

$$\frac{\Sigma_i(d+2)}{\Sigma_i(d)} = R_{ii}(d) \quad (\text{B.4})$$

Then defining the rescaled integrals $J_i(d) = I_i(d)/\Sigma_i(d)$ and $r_i(d) = \sum_{j \neq i} R_{ij} J_j(d)/\Sigma_i(d)$ the recurrence relation (B.1) becomes

$$\mathbf{J}(d+2) = \mathbf{J}(d) + \mathbf{r}(d). \quad (\text{B.5})$$

The general solution to (B.5) consists of a homogeneous and a inhomogeneous solution $\mathbf{J}(d) = \mathbf{J}_{\text{hom}}(d) + \mathbf{J}_{\text{inhom}}(d)$.

The homogeneous solution $\mathbf{J}_{\text{hom}}(d) = \mathbf{f}(d)$ can be any periodic in d with period 2: $\mathbf{f}(d+2) = \mathbf{f}(d)$. Since the product $f_i(d)\Sigma_i(d)$ must obey the bound (B.3), choosing Σ_i such that it comes as close as possible to saturating it maximally constrains the form of f_i . In particular, it is always possible to find a Σ_i such that (B.3) forces $|f(d)| < |\text{Im } d|^\nu e^{\pi|\text{Im } d|}$ for some ν . Then, the only 2-periodic function of d that satisfy this bound is cot (or tan). Thus, f_i has the following form

$$f_i(d) = b_{i0} + \sum_j^{n_{ij}} \sum_{k=1}^L b_{ijk} \cot^k \left(\frac{\pi}{2} (d - q_{ij}) \right) \quad (\text{B.6})$$

where the q_{ij} are poles that appear in $J_{i,\text{inhom}}$, n_{ij} is the number of distinct q_{ij} and L is the maximal order of any pole. Then, the b_{ijk} 's are fixed by requiring that I_i is free from all poles in the strip S_i .

Sometimes, this requirement will not fix all b_{ijk} 's and one has to generate additional conditions. Additional conditions can be generated by relating I_i to \tilde{I}_i via an IBP relation and then requiring that \tilde{I}_i is pole free in its strip \tilde{S}_i . For example, squaring all propagators defines an integral with a larger finite strip. Since this new integral is related to the old integral via an IBP relation, requiring that the new integral is free from all poles in its enlarged strip may impose new constraints on the old integral.

To obtain the inhomogeneous solution, we split $r_i(d)$ into two pieces $r_i(d) = r_i^+(d) + r_i^-(d)$ where $r_i^+(d+2k) \sim a^k$ and $r_i^-(d-2k) \sim a^k$ in the large k limit with $0 < a < 1$. Then, the inhomogeneous solution $\mathbf{J}_{\text{inhom}}(d) = \mathbf{g}(d)$ becomes

$$g_i(d) = \sum_{k=0}^{\infty} r_i^+(d+2k) + \sum_{k=1}^{\infty} r_i^-(d-2k). \quad (\text{B.7})$$

Since each term in the sum is suppressed by some a^k this series converges exponentially. While each integral in the family usually contributes only to r^+ or r^- sometimes it is necessary to split an integral into two pieces (this will be the case for $I_1^{(3)}$).

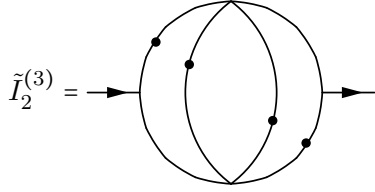
This method expresses integrals in terms of (nested) sums that converge rapidly. In practice, one computes these sums numerically to many digits and then applies the PSLQ algorithm to recover analytic results.

B.2 Computing $I_1^{(3)}$ and $I_2^{(3)}$

Using the formalism outlined in the previous section, we evaluate the integrals $I_1^{(3)}$ and $I_2^{(3)}$ for $d = 3$.

Before being able to apply the methods from section B.1, we must check if $I_1^{(3)}$ and $I_2^{(3)}$ have a strip of width at least two that is free from poles. The integral $I_1^{(3)}$ has a strip of width two: $S_1 = \{d \in \mathbb{C} | \frac{10}{3} < \text{Re } d < \frac{16}{3}\}$ where $d = \frac{16}{3}$ is the minimal UV divergence and $d = \frac{10}{3}$ is the maximal IR divergence. On the other hand, $I_2^{(3)}$ does not have a strip of width two since its minimal UV divergence is at $d = 4$ and its maximal IR divergence is at $d = \frac{8}{3}$.

In order to use the methods of the previous section, we replace $I^{(3)}$ by the related integral



$$\tilde{I}_2^{(3)} = \text{Diagram} \quad (\text{B.8})$$

where each dotted propagator is squared. By selectively squaring the propagators of $I_2^{(3)}$, we have enlarged the strip S_2 to $\tilde{S}_2 = \{d \in \mathbb{C} | \frac{14}{3} < \text{Re } d < \frac{20}{3}\}$. Once $\tilde{I}_2^{(3)}$ is known $I_2^{(3)}$ is determined via the IBP relation

$$I_2^{(3)}(p^2; d) = \frac{16(d-5) (p^2)^2 \tilde{I}_2^{(3)}(p^2; d)}{3(d-3)(3d-14)(3d-10) U(d)} - \frac{4(2d-5)(3d-8) T(d) (p^2)^{-1} I_6^{(3)}(p^2; d)}{3(d-6)^2(d-5)(d-4)^2(3d-14)(3d-10) U(d)}, \quad (\text{B.9})$$

where

$$U(d) = 3d^2 - 33d + 92, \quad (\text{B.10})$$

$$T(d) = 3429d^7 - 109566d^6 + 1491897d^5 - 11216508d^4 + 50262008d^3 - 134170880d^2 + 197449040d - 123506880. \quad (\text{B.11})$$

Now, we can define a new family of integrals

$$\mathbf{I}' = \left(\frac{I_1^{(3)}}{(p^2)^{\omega_1}}, \frac{\tilde{I}_2^{(3)}}{(p^2)^{\omega_2}}, \frac{I_3^{(3)}}{(p^2)^{\omega_3}}, \dots, \frac{I_6^{(3)}}{(p^2)^{\omega_6}} \right) \quad (\text{B.12})$$

for which the formalism of section B.1 is applicable. Normalizing by $(p^2)^{-\omega_i}$ where ω_i is the superficial degree of divergence of $I_i^{(3)}$, ensures that the basis \mathbf{I}' is dimensionless. This family of integrals satisfies the recurrence relation

$$\mathbf{I}'(d+2) = \underline{\mathbf{R}}(d) \cdot \mathbf{I}'(d). \quad (\text{B.13})$$

where $\underline{\mathbf{R}}(d)$ is a lower triangular 6×6-matrix. We also define the following summing factors that (almost) saturate the bound (B.3)

$$\Sigma'_1(d) = \frac{1}{(4\pi)^{\frac{d}{2}}} \left(\frac{7}{2} - d\right) \Gamma(6 - 2d) \Gamma\left(\frac{d}{2} - 2\right), \quad (\text{B.14})$$

$$\Sigma'_2(d) = \frac{U(d) \Gamma\left(\frac{3}{2} - \frac{d}{2}\right) \Gamma\left(\frac{8}{3} - \frac{d}{2}\right) \Gamma\left(\frac{10}{2} - \frac{d}{2}\right) \sec\left(\frac{\pi}{2}d\right)}{4^d 3^{\frac{3d}{2}} \pi^{\frac{d}{2}} (d-5)}. \quad (\text{B.15})$$

With this, the inhomogeneous solutions are given by (B.7). We remark here that $r_2^- = 0$ and r_1^- only receives contribution from the homogeneous solution of I'_2 . All other integrals contributes to r_1^+ and r_2^- .

The final piece is the homogeneous solutions

$$f'_1(d) = -\frac{16\pi^3}{9} \left[-15 \cot^3\left(\frac{\pi}{2}(d-4)\right) + 16 \cot\left(\frac{\pi}{2}(d-4)\right) + 9 \cot\left(\frac{\pi}{2}(d-5)\right) - 2 \cot\left(\frac{\pi}{2}\left(d - \frac{10}{3}\right)\right) - 2 \cot\left(\frac{\pi}{2}\left(d - \frac{14}{3}\right)\right) \right], \quad (\text{B.16})$$

$$f'_2(d) = 2187\sqrt{3} \pi^{\frac{3}{2}} \cot\left(\frac{\pi}{2}(d-6)\right) \left(1 - \cot^2\left(\frac{\pi}{2}(d-6)\right)\right). \quad (\text{B.17})$$

While requiring I'_2 to be free of poles in the strip \tilde{S}_2 fixes all the coefficients of f'_2 , requiring I'_1 to be free from poles in S_1 leaves one coefficient of f'_1 unfixed. The remaining coefficient was fixed by requiring the integral obtained by squaring all propagators of I'_1 , which is related to I'_1 by IBP relations, to be free from poles in its strip.

Putting all the pieces together yields expressions for I'_1 and I'_2

$$I'_{i=1,2}(d) = \Sigma'_i(d) [f'_i(d) + g'_i(d)]. \quad (\text{B.18})$$

For a given d , the infinite sum in g'_i can be truncated and evaluated numerically. Then, analytic expressions for I'_1 and I'_2 are recovered using the PSLQ algorithm.

Once I'_1 and I'_2 are known for a given d , we can determine the integrals we actually need

$$\begin{aligned} I_1^{(3)}(p^2; d) &= (p^2)^{\omega_1} I'_1(p^2; d), \\ I_2^{(3)}(p^2; d) &= \frac{16(3-5) (p^2)^{2+\tilde{\omega}_2} I'_2(p^2; d)}{3(3-3)(3d-14)(3d-10) U(d)} \\ &\quad - \frac{4(2d-5)(3d-8) T(d) (p^2)^{\tilde{\omega}_2-1} I_6^{(3)}(p^2; d)}{3(d-6)^2(d-5)(d-4)^2(3d-14)(3d-10) U(d)}. \end{aligned} \quad (\text{B.19})$$

Here, we have used the IBP relation (B.9) and the definition of the primed-basis (B.12). For $d = 3$, we find (A.11).

C Ingredients for on-shell calculations

In this appendix we presents further details for obtaining the results of sections 2.2 and 5.3.

C.1 Stress-Tensor gluon form factors

In this section we discuss the derivation of eq. (2.22) using BCFW method [36, 37]. We start by writing the form factor $\langle p_1^g p_2^g | T^{\mu\nu}(p) | 0 \rangle$ in four-dimensions using spinor-helicity variables,

$$\langle p_1^- p_2^+ | T^{\mu\nu}(p) | 0 \rangle^{4d} = \delta^{ab} \frac{\langle 1^{\dot{\alpha}} \langle 1^{\dot{\beta}} \langle 1^{\dot{\gamma}} p_{\dot{\gamma}}^{\alpha} \sigma_{\alpha\dot{\alpha}}^{\mu} \langle 1^{\dot{\rho}} p_{\dot{\rho}}^{\beta} \sigma_{\beta\dot{\beta}}^{\nu} \rangle \rangle \rangle}{\langle 12 \rangle^2}, \quad (\text{C.1})$$

where α, β, γ and ρ (and their dotted) version indices are $SU(2)$ indices. We can then obtain $\langle p_1^+ p_2^+ p_3^- | T^{\mu\nu}(p) | 0 \rangle$ by shifting p_3 and p_2 as follows,

$$[\hat{2}] = [2] \quad [\hat{3}] = [3] + z[2] \quad |\hat{2}\rangle = |2\rangle - z|3\rangle \quad |\hat{3}\rangle = |3\rangle, \quad (\text{C.2})$$

The on-shell form factor is then given as:

$$\langle p_1^+ p_2^+ p_3^- | T^{\mu\nu}(p) | 0 \rangle^{4d} = \langle \hat{P}_{12}^+ \hat{p}_3^- | T^{\mu\nu}(p) | 0 \rangle \frac{1}{P_{12}^2} M_3(p_1^+, \hat{p}_2^2, -\hat{P}_{12}^-) \quad (\text{C.3})$$

where the 3-gluon on-shell form factor can be written as,

$$M_3(p_1^+, \hat{p}_2^2, -\hat{P}_{12}^-) = g_s f^{bcd} \frac{[\hat{1}\hat{2}]^3}{[1\hat{P}_{12}][\hat{2}\hat{P}_{12}]}. \quad (\text{C.4})$$

With the little bit manipulation eq. (C.3) can be written as,

$$\langle p_1^+ p_2^+ p_3^- | T^{\mu\nu}(p) | 0 \rangle^{4d} = 2g_s f^{bcd} \frac{\langle 3 | \langle 3 | \langle 3 p \sigma^{\mu} \langle 3 p \sigma^{\nu} \rangle \rangle \rangle}{\langle 12 \rangle \langle 23 \rangle \langle 31 \rangle}. \quad (\text{C.5})$$

Here we omitted the $SU(2)$ indices. To go to three dimensions, we use the relation between 3d and 4d polarization, i.e., $\epsilon^{3d} = \frac{\epsilon^+ + \epsilon^-}{2}$. This yields the result in eq. (2.22).

C.2 Phase space integrals

In this section we discuss the phase space integral yielding the non-analytic part of the two-loop results in sections 2.2 and 5.3. As discussed in the main text in section 2.2, the only cut diagram contributing to non-analytic two loop results is the most right diagram in figure 3. So the on-shell form factors needed for two loop calculations are $\langle p_1^g p_2^g p_3^g | O | 0 \rangle$.

We can calculate the discontinuity by gluing sides of the diagram in 3 together using,

$$\begin{aligned} \text{Disc}(\langle OO' \rangle) &= (2f^{abc} g_s)^2 \frac{-i}{3!} \int \frac{d^2 p_1}{(2\pi)^2 2E_1} \frac{d^2 p_2}{(2\pi)^2 2E_2} \frac{d^2 p_3}{(2\pi)^2 2E_3} \\ &\times (2\pi)^3 \delta^3(p - p_1 - p_2 - p_3) \langle 0 | O(p) | p_1^g p_2^g p_3^g \rangle \langle p_1^g p_2^g p_3^g | O'(p) | 0 \rangle. \end{aligned} \quad (\text{C.6})$$

We can then do the projection to different spin at this level to obtain the integrands which are scalar functions of p_1, p_2 and p_3 ,

$$\text{Disc} A_j^{(1)} = -i g_s^2 C_A \frac{16}{3\pi^3} \int \frac{d^2 p_1}{E_1} \frac{d^2 p_2}{E_2} \frac{d^2 p_3}{E_3} \delta^3(p - p_1 - p_2 - p_3) I_j(p_1, p_2, p_3). \quad (\text{C.7})$$

To do the integral, we go to the rest frame of p and define the usual parameters for 3-body phase space calculation,

$$p = (p^0, 0, 0), \quad x_i = \frac{p_i \cdot p}{p^2}, \quad x_1 + x_2 + x_3 = 1. \quad (\text{C.8})$$

Now we can write $I_j(p_1, p_2, p_3)$ in terms of x_i s. Further, using spatial δ -function we can integrate x_3 trivially and write the remaining integrals as,

$$\text{Disc}A_j^{(1)} = ig_s^2 C_A \frac{16}{3\pi^3} \int \frac{d^2x_1}{x_1^2} \frac{d^2x_2}{x_2^2} \delta(\theta - \theta_*) \frac{I_j(x_1, x_2)}{\sin \theta_*}, \quad (\text{C.9})$$

where $\cos \theta_* = (1/2 + x_1x_2 - x_2 - x_1)/x_1x_2$. Now the angular integrals can be done and we are left with the two one-dimensional integrals:

$$\text{Disc}A_j^{(1)} = ig_s^2 C_A \frac{16}{3\pi^2} \int_{\frac{1}{2}-x_1}^{\frac{1}{2}} dx_2 \int_0^{\frac{1}{2}} dx_1 \frac{x_1^2 x_2^2 I_j(x_1, x_2)}{(\frac{1}{2} - x_1)(\frac{1}{2} - x_2)(x_1 + x_2 - \frac{1}{2})}. \quad (\text{C.10})$$

These integrals can then be simply calculated to obtain the non-analytic two loop results quoted in the paper.

References

- [1] S. Weinberg, *Precise relations between the spectra of vector and axial vector mesons*, *Phys. Rev. Lett.* **18** (1967) 507–509.
- [2] M. A. Shifman, A. I. Vainshtein and V. I. Zakharov, *QCD and Resonance Physics. Theoretical Foundations*, *Nucl. Phys. B* **147** (1979) 385–447.
- [3] M. A. Shifman, ed., *Vacuum structure and QCD sum rules*. North-Holland, 1992.
- [4] M. Shifman, *Vacuum structure and QCD sum rules: introduction*, .
- [5] D. Karateev, S. Kuhn and J. a. Penedones, *Bootstrapping Massive Quantum Field Theories*, *JHEP* **07** (2020) 035, [[1912.08940](#)].
- [6] M. Correia, J. Penedones and A. Vuignier, *Injecting the UV into the Bootstrap: Ising Field Theory*, [2212.03917](#).
- [7] M. Teper, *SU(N(c)) gauge theories for all N(c)*, *Nucl. Phys. B Proc. Suppl.* **53** (1997) 715–718, [[hep-lat/9701004](#)].
- [8] M. J. Teper, *SU(n) gauge theories in 2+1 dimensions*, *Phys. Rev. D* **59** (Dec, 1998) 014512.
- [9] D. Diakonov and V. Petrov, *Yang-Mills theory in three-dimensions as quantum gravity theory*, *J. Exp. Theor. Phys.* **91** (2000) 873–893, [[hep-th/9912268](#)].
- [10] B. Lucini and M. Teper, *SU(N) gauge theories in (2+1)-dimensions: Further results*, *Phys. Rev.* **D66** (2002) 097502, [[hep-lat/0206027](#)].
- [11] H. B. Meyer and M. J. Teper, *High spin glueballs from the lattice*, *Nucl. Phys.* **B658** (2003) 113–155, [[hep-lat/0212026](#)].
- [12] H. B. Meyer and M. J. Teper, *Glueball Regge trajectories in (2+1)-dimensional gauge theories*, *Nucl. Phys.* **B668** (2003) 111–137, [[hep-lat/0306019](#)].

- [13] B. Bringoltz and M. Teper, *A precise calculation of the fundamental string tension in $su(n)$ gauge theories in 2+1 dimensions*, *Phys. Lett. B* **645** (2007) 383–388, [[hep-th/0611286](#)].
- [14] F. Buisseret, V. Mathieu and C. Semay, *(2 + 1)-d Glueball Spectrum within a Constituent Picture*, *Eur. Phys. J. C* **73** (2013) 2504, [[1301.3247](#)].
- [15] F. Bursa, R. Lau and M. Teper, *$So(2n)$ and $su(n)$ gauge theories in 2+1 dimensions*, *JHEP* **05** (2013) 025, [[1208.4547](#)].
- [16] A. Athenodorou and M. Teper, *Closed flux tubes in $d = 2 + 1$ $su(n)$ gauge theories: dynamics and effective string description*, *JHEP* **10** (2016) 093, [[1602.07634](#)].
- [17] A. Athenodorou and M. Teper, *$SU(N)$ gauge theories in 2+1 dimensions: glueball spectra and k -string tensions*, *JHEP* **02** (2017) 015, [[1609.03873](#)].
- [18] R. Lau and M. Teper, *$So(n)$ gauge theories in $2 + 1$ dimensions: glueball spectra and confinement*, *JHEP* **10** (2017) 022, [[1701.06941](#)].
- [19] M. Teper, *$So(4)$, $so(3)$ and $su(2)$ gauge theories in 2+1 dimensions: comparing glueball spectra and string tensions*, [1801.05693](#).
- [20] P. Conkey, S. Dubovsky and M. Teper, *Glueball spins in $d = 3$ yang-mills*, *JHEP* **10** (2019) 175, [[1909.07430](#)].
- [21] V. L. Chernyak and A. R. Zhitnitsky, *Asymptotic Behavior of Hadron Form-Factors in Quark Model. (In Russian)*, *JETP Lett.* **25** (1977) 510.
- [22] G. P. Lepage and S. J. Brodsky, *Exclusive Processes in Quantum Chromodynamics: The Form-Factors of Baryons at Large Momentum Transfer*, *Phys. Rev. Lett.* **43** (1979) 545–549.
- [23] S. J. Brodsky, Y. Frishman, G. P. Lepage and C. T. Sachrajda, *Hadronic Wave Functions at Short Distances and the Operator Product Expansion*, *Phys. Lett. B* **91** (1980) 239–244.
- [24] V. L. Chernyak, A. A. Ogloblin and I. R. Zhitnitsky, *On the Nucleon Wave Function*, *Sov. J. Nucl. Phys.* **48** (1988) 536.
- [25] G. Policastro, D. T. Son and A. O. Starinets, *From AdS / CFT correspondence to hydrodynamics. 2. Sound waves*, *JHEP* **12** (2002) 054, [[hep-th/0210220](#)].
- [26] A. Hietanen, K. Kajantie, M. Laine, K. Rummukainen and Y. Schroder, *Plaquette expectation value and gluon condensate in three dimensions*, *JHEP* **01** (2005) 013, [[hep-lat/0412008](#)].
- [27] F. Di Renzo, M. Laine, V. Miccio, Y. Schroder and C. Torrero, *The Leading non-perturbative coefficient in the weak-coupling expansion of hot QCD pressure*, *JHEP* **07** (2006) 026, [[hep-ph/0605042](#)].
- [28] V. A. Novikov, M. A. Shifman, A. I. Vainshtein and V. I. Zakharov, *Wilson’s Operator Expansion: Can It Fail?*, *Nucl. Phys. B* **249** (1985) 445–471.
- [29] J. Zinn-Justin, *Quantum field theory and critical phenomena*, *Int. Ser. Monogr. Phys.* **113** (2002) 1–1054.
- [30] M. A. Shifman, *Vacuum structure and QCD sum rules*. Elsevier, 1992.
- [31] K. Kajantie, M. Laine, K. Rummukainen and Y. Schroder, *The Pressure of hot QCD up to $g^6 \ln(1/g)$* , *Phys. Rev. D* **67** (2003) 105008, [[hep-ph/0211321](#)].
- [32] A. V. Smirnov and F. S. Chuharev, *FIRE6: Feynman Integral REduction with Modular Arithmetic*, [1901.07808](#).

- [33] M. E. Peskin and D. V. Schroeder, *An Introduction to quantum field theory*. Addison-Wesley, Reading, USA, 1995.
- [34] M. Srednicki, *Quantum Field Theory*. Cambridge University Press, 2007, [10.1017/CBO9780511813917](#).
- [35] M. D. Schwartz, *Quantum Field Theory and the Standard Model*. Cambridge University Press, 3, 2014.
- [36] R. Britto, F. Cachazo, B. Feng and E. Witten, *Direct proof of tree-level recursion relation in Yang-Mills theory*, *Phys. Rev. Lett.* **94** (2005) 181602, [[hep-th/0501052](#)].
- [37] R. Britto, F. Cachazo and B. Feng, *New recursion relations for tree amplitudes of gluons*, *Nucl. Phys. B* **715** (2005) 499–522, [[hep-th/0412308](#)].
- [38] K. G. Chetyrkin, A. L. Kataev and F. V. Tkachov, *New Approach to Evaluation of Multiloop Feynman Integrals: The Gegenbauer Polynomial x Space Technique*, *Nucl. Phys.* **B174** (1980) 345–377.
- [39] K. G. Chetyrkin and F. V. Tkachov, *Integration by Parts: The Algorithm to Calculate beta Functions in 4 Loops*, *Nucl. Phys.* **B192** (1981) 159–204.
- [40] P. A. Baikov and K. G. Chetyrkin, *Four Loop Massless Propagators: An Algebraic Evaluation of All Master Integrals*, *Nucl. Phys.* **B837** (2010) 186–220, [[1004.1153](#)].
- [41] R. N. Lee, *Space-time dimensionality D as complex variable: Calculating loop integrals using dimensional recurrence relation and analytical properties with respect to D* , *Nucl. Phys. B* **830** (2010) 474–492, [[0911.0252](#)].
- [42] M. F. Paulos, J. Penedones, J. Toledo, B. C. van Rees and P. Vieira, *The S -matrix bootstrap II: two dimensional amplitudes*, *JHEP* **11** (2017) 143, [[1607.06110](#)].
- [43] M. F. Paulos, J. Penedones, J. Toledo, B. C. van Rees and P. Vieira, *The S -matrix bootstrap. Part III: higher dimensional amplitudes*, *JHEP* **12** (2019) 040, [[1708.06765](#)].
- [44] M. S. Costa, J. Penedones, D. Poland and S. Rychkov, *Spinning Conformal Correlators*, *JHEP* **11** (2011) 071, [[1107.3554](#)].
- [45] M. Kologlu, P. Kravchuk, D. Simmons-Duffin and A. Zhiboedov, *Shocks, Superconvergence, and a Stringy Equivalence Principle*, *JHEP* **11** (2020) 096, [[1904.05905](#)].
- [46] S. Caron-Huot, Y.-Z. Li, J. Parra-Martinez and D. Simmons-Duffin, *Causality constraints on corrections to Einstein gravity*, *JHEP* **05** (2023) 122, [[2201.06602](#)].
- [47] P. D. Anderson and M. Kruczenski, *Loop Equations and bootstrap methods in the lattice*, *Nucl. Phys. B* **921** (2017) 702–726, [[1612.08140](#)].
- [48] V. Kazakov and Z. Zheng, *Bootstrap for lattice Yang-Mills theory*, *Phys. Rev. D* **107** (2023) L051501, [[2203.11360](#)].